Strain Engineering of Perpendicular Magnetic Insulators for Magnetoelectronics

by

Nguyen Vu

A dissertation submitted in partial fulfillment
of the requirements for the degree of
Doctor of Philosophy
(Materials Science and Engineering)
in The University of Michigan
2021

Doctoral Committee:

Professor John Heron, Chair
Professor Robert Hovden
Professor Yiyang Li
Professor Liuyan Zhao

"Let this be the hour when we draw swords together.
Fell deeds awake.
Now for wrath, now for ruin, and the red dawn.
Forth, Eorlingas!"

Theoden, Lord of the Rings

Nguyen M. Vu

nguyenvu@umich.edu

ORCID iD: 0000-0003-2782-1506

©Nguyen M.Vu 2021

Acknowledgements

This thesis was made possible by the intellectual and financial support from many of my colleagues, collaborators and sponsors. I thank Peter Meisenheimer for supporting the rebuttal process for the $Tm_3Fe_5O_{12}$ manuscript, including refining magnetometry data and performing XPS measurements. I thank Professor Liuyan Zhao in Physics department and her students, Xiangpeng Luo and Dr. Wencan Jin for their second harmonic measurement of Cr_2O_3 samples. I thank Professor Robert Hovden in Materials Science department for the use of his lab's instruments and Professor Lu Li in Physics department for the use of their Physical Property Measurement System. I thank Dr. Morgan Trassin and Johanna Nordlander at ETH Zurich for their initial support in second harmonic measurement of Cr_2O_3 thin film. I thank Matthew Webb for his XPS measurement of Boron concentration, Tony Chiang for his help in dielectric testing of the Boron doped series and Sieun Chae for her DFT defect formation calculation. I thank Professor Yiyang Li in Materials Science department for his enthusiasm and advice he has given me during and after my data meeting talk. I thank Steve Novakov for his support in device fabrication as well as the homemade transport system he built which initiates the early Néel temperature measurement. Last but not least, I thank my advisor John Heron for his guidance throughout my Ph.D. and his infinite patience in fixing my thesis. My studies at Michigan are funded by the Vietnam Education Foundation, the Rackham Graduate School, the College of Engineering and the Semiconductor Research Corporation (NewLimits center).

Table of Contents

Acknowledgements **ii**

List of Figures **v**

List of Tables **xii**

List of Abbreviations **xiii**

Abstract **xiv**

Chapter 1: Perpendicular Magnetic Insulators Towards Energy Efficient Electronics **1**

1.1 Spin current switching of magnetic orientation in magnetic insulators 3

1.2 Electric field control of magnetism 6

Chapter 2: Experimental Methods **9**

2.1 Pulsed Laser Deposition 9

2.2 X-ray diffraction 14

2.3 Vibrating sample magnetometer 18

2.4 Magneto-transport 20

2.5 Second harmonic generation 23

Chapter 3: Strain Tuning in Ferrimagnet $Tm_3Fe_5O_{12}$ **24**

3.1 Background: Magnetic anisotropy 24

3.2 The growth of $Tm_3Fe_5O_{12}$ 28

3.3 Strain tuning through structural characterization 29

3.4 Anisotropy tuning 30

Chapter 4: Magneto-electrics Cr_2O_3 **39**

4.1 Background 39

4.1.1 Crystal structure and magnetic structure 39

4.1.2 Magneto-electricity in Cr_2O_3 40

4.1.3 Exchange bias in heterostructures 43

4.1.4 Magnetic proximity effect 46

4.2 Single-crystal growth of Cr_2O_3 on an electrode 47

4.3 Electrical properties of sub 100-nm-thin Cr_2O_3 film 51

4.4 Magnetic properties of sub 100-nm-thin Cr_2O_3 film 52

4.5 Néel temperature investigation 54

Chapter 5: Conclusions and Recommendations for Future Work **58**

5.1 Boron doping of Cr_2O_3 59

5.2 Electrical switching in sub 100-nm-thin Cr_2O_3 60

Bibliography **63**

List of Figures

1.0.1 **(a)** Frequency scaling progress over the year. **(b)** Apply voltage scaling with device size. Images reprinted with permission from [1]. 2

1.0.2 Stable state of magnetic memory cells is in perpendicular configuration, adapted from [2]. 2

1.1.1 **(a)** Hysteresis of a ferromagnet, showing the definitions of saturation magnetization M_s and coercive field H_c, adapted from [3]. **(b)** Out-of-plane (OOP) and in-plane (IP) magnetometery of a perpendicular magnet (Pt/Co/Pt), stating the definition of anisotropy field H_K, which is the field needed to rotate the magnetization from easy axis to hard axis. **(c)** Anisotropy energy explanation. **(d)** Torques acting on magnetization **m** cause a precessional motion, adapted from [2]. 4

1.2.1 **(a)** Leakage current of $500\,nm$ thick Cr_2O_3, reprinted with permission from [4]. High angular annular dark field scanning transmission electron microscopy of **(b)** plan view along [0001] of Cr_2O_3 on Al_2O_3, showing crystallographic domains (the inset shows higher resolution image), and **(c)** domain boundary atomic structure along $[11\bar{2}0]$, reprinted with permission from [5]. 8

2.1.1 **(a)** Schematic of pulsed laser deposition. **(b)** Plasma plumes at different background gas pressures. High resolution X-ray diffraction showing Laue oscillation of **(c)** Pt deposited on YSZ (111) with Ti buffer layer, reprinted with permission from [6], and **(d)** Entropy-stabilized oxide deposited on MgO (001) $(Mg_{0.25(1-x)}Co_xNi_{0.25(1-x)}Cu_{0.25(1-x)}Zn_{0.25(1-x)})O$, adapted from [7], indicates highly crystalline and smooth thin films grown by pulsed laser deposition (PLD). 10

2.1.2 **(a)** Growth modes in thin film, energy ratio is defined as $\Phi_{fs}/\Phi_{ss} - 1$, with Φ is interatomic potential of film-substrate or substrate-substrate, adapted from [8, 9]. **(b)** Topography changes with oxygen pressure in Cr_2O_3 grown on (001) Al_2O_3. **(c)** $La_{0.7}Sr_{0.3}MnO_3$ grown on (001) $SrTiO_3$ changes its growth mode with laser fluence, printed with permission from [10]. **(d)** Topography of $SrRuO_3$ grown on (100) $SrTiO_3$ at different temperatures (from left to right: 688, 642, 592^oC), adapted from [11]. 12

2.2.1 **(a)** Symmetric X-ray diffraction. **(b)** Standard axes in Rigaku Smartlab diffractometer. Adapted from [12]. 15

2.2.2 Information provided by X-ray reflectivity, adapted from [13]. 16

2.2.3 **(a)** ϕ scan of (1,0,10) plane in thin film Cr_2O_3 grown on different substrates, adapted from [14]. **(b)** 3-fold symmetry of (001) plane in Cr_2O_3 and 60^o rotation of the crystal around [001] axis (Crystal structure was constructed using Vesta software). 17

2.2.4 **(a)** Relations of distances in reciprocal space and real space, demonstrated for Ge film grown on Si (001) substrate, a_p and a_n are in-plane and out-of-plane lattice parameters, adapted from [15]. **(b)** Reciprocal space mapping of (113) plane of $Si_{0.74}Ge_{0.26}$ grown on Si (001) substrate, **left** is fully strained lattice and **right** is partial relaxed lattice, printed with permission from [16]. 19

2.3.1 Typical VSM setup and sample holders for a Lakeshore system, adapted from [17]. 20

2.4.1 Transport setup within the Lakeshore magnet. 21

2.4.2 **(a)** Schematics of Hall measurement, adapted form [18]. **(b)** Spinning current method. 22
2.4.3 **(a)** Sample stack for dielectric testing. **(b)** Device stack for Hall measurement. 22
2.5.1 Typical second harmonic measurement setup in transmission mode. The incident probe beam is linearly polarized with polarization direction defined by the polarizer angle. The polarization direction of the detected second harmonic signal is projected along the analyzer angle. Adapted from [19]. . . . 23

3.1.1 **Left**: Polyhedra in one unit cell of $Tm_3Fe_5O_{12}$. **Right**: Zoom-in corner of the unit cell, showing individual Fe^{3+} ions occupy tetrahedral and octahedral sites. Dashed lines represent unit cell (Crystal structure was constructed using Vesta software). 25
3.3.1 **(a)** Schematics of strain in $Tm_3Fe_5O_{12}$ (TmIG) thin film caused by lattice mismatch with the substrate. **(b)** Symmetric X-ray diffraction around 444 peak of 17 nm thick (111) TmIG grown on different substrates. **(c)** Reciprocal space mapping around 444 diffraction peak of both film and substrate. Adapted from [20]. 32
3.3.2 Zoom-in of Reciprocal space mapping (RSM) scans in NGG and GSGG substrates, showing a slight relaxation in the film lattice, adapted from [21]. . . 33
3.3.3 X-ray reflectivity of TmIG on different substrates, solid back lines are fitting data, adapted from [21]. 33
3.3.4 Topography of the TmIG films grown on different substrates, adapted from [21]. 34
3.4.1 **(a)** Room temperature out-of-plane magnetization versus magnetic field of 17 nm TmIG thin film on different substrate. **(b)** Saturation magnetization versus distortion angle β. Adapted from [20]. 35

3.4.2 **Top row** Room temperature, in-plane magnetization vesrus magnetic field scans of 17 nm TmIG grown on different substrates. The open circle is experimental data and the black line is fitted data following the Stoner-Wohlfarth microspin model. The curvature of the hysteresis loop is from an 5^o offset from the in-plane hard axis due to experimental setup. **Middle row** First derivative of in-plane loops (points), shown with first derivative of the calculated fits (black line). **Bottom row** Second derivative of the fitted data in top row. Anisotropy field is determined from the peaks of second derivative with a field resolution of 1 Oe. Adapted from [21]. 36

3.4.3 **(a)** Anisotropy field H_K, **(b)** magnetoelastic energy K_{me}, **(c)** magnetoelastic constant B_2 and **(d)** device size as a function of distortion angle, adapted from [21]. 37

3.4.4 X-ray photonelectron spectroscopy data of TmIG target and thin films on different substrates. **(a)** Raw data and **(b)** estimated ratio of Fe and Tm element in each sample, adapted from [21]. 38

4.1.1 **(a)** Crystal structure belong to rhombohedral family with 4 Cr^{3+} atoms aligning along c axis. **(b)** Magnetic structure of Cr_2O_3: each Cr^{3+} atom is surrounded by an oxygen octahedron and has spin pointing parallel to each other and perpendicular to the c axis. (Crystal structure was constructed using Vesta software) **(c)** Configuration of surface magnetization of Cr_2O_3, printed with permissions from [22]. 40

4.1.2 Schematic of magnetization switching using electric field using magnetoelectric materials. Since the material possess magnetoelectric effect, applying an electric field can switch its magnetization. The ferromagnetic layer on top is also switched in this process through exchange coupling and is used to probe the change in magnetization of magnetoelectric layer. 44

4.1.3 **(a)** Proximity effect in Pt/Cr_2O_3 heterostructure and anomalous Hall setup using spinning current offset method. **(b)** Invariant Hall resistance reflect the net magnetic moment at zero applied field. At temperature above Néel temperature, only a small magnetic field needed to saturate the moment in Pt layer. **(c)** Néel temperature detection in Cr_2O_3 using the anomalous Hall voltage. The thickness of Cr_2O_3 film in this work is $250\,nm$. Printed with permission from [23]. 47

4.2.1 **(a)** X-ray diffraction of thin film Cr_2O_3 grown on (0001) Al_2O_3, oscillation fringes around the film peaks indicates good crystallinity, **(b)** Phi scan around 014 peak of Cr_2O_3 shows 3-fold symmetry which is signature of single domain crystal, **(c)** X-ray reflectivity of the film. 48

4.2.2 X-ray diffraction of **(a)** Pt grown on STO (111) and **(b)** Pt grown on YSZ (111) with Ti buffer layer. Insets are zoom-in plots around the Pt (111) peak, revealing oscillation fringes which indicate smooth surface and high crystallinity. 49

4.2.3 Φ scan of Pt and Cr_2O_3 **(a)** 1% twin Pt grown on STO (111) substrate, **(b)** twin Pt grown on YSZ (111) with Ti buffer layer, showing a 30^o rotation in Cr_2O_3 lattice, **(c)** single crystal Pt grown on YSZ (111) with Ti buffer layer. 49

4.2.4 Crystal structure of Pt (**left**), Cr_2O_3 (**middle**) and calculated strains for different orientations of Pt with respect to Cr_2O_3 lattice (**right**). 50

4.2.5 **(a)** X-ray diffraction of Cr_2O_3 grown on V_2O_3, Cr_2O_3 was grown in oxygen, the peak indicates the formation of VO_2 phase. **(b)** V_2O_3 oxidized into V_2O_5 and melted at the edge. 50

4.2.6 **(a)** Zoom-in X-ray diffraction scan of Cr_2O_3 grown on V_2O_3 on Al_2O_3 (0001) substrate. **(b)** Fitting of the V_2O_3 peak with the full width half max value w and peak position x_c. 51

4.2.7 **(a)** Full range X-ray diffraction of Cr_2O_3 grown on V_2O_3 on Al_2O_3 (0001) substrate. **(b)** ϕ scan around Cr_2O_3 014 showing a 3-fold symmetry. **(c)** Topography of Cr_2O_3 grown on V_2O_3 with surface roughness $0.083\,nm$. Adapted from [21]. 51

4.3.1 **(a)** Mean resistivity of 60 nm thick Cr_2O_3 (blue), 30 nm thick Cr_2O_3 (yellow) on (0001)-oriented V_2O_3/Al_2O_3 and 70 nm thick Cr_2O_3 on (111)-oriented Pt/Ti/YSZ (orange). The black dash line is the bulk value. **(b)** Breakdown electric field of low leakage devices in 60 nm thick Cr_2O_3 (top panel), 30 nm thick Cr_2O_3 on V_2O_3/Al_2O_3 (middle panel), and 70 nm thick Cr_2O_3 on Pt/Ti/YSZ (bottom panel) at different electrode diameters. Adapted from [21]. 53

4.4.1 **(a)** Optical second harmonic generation intensity from a 30-nm-thick Cr_2O_3 on V_2O_3 electrode at room temperature (orange: analyzer along the x-direction ($[11\bar{2}0]$), blue: analyzer along y-direction ($[\bar{1}100]$)) and theoretical plot of electric dipole signal (Equation (4.4.0.2)) when analyzer is fixed along x-direction (dash-orange) and y-direction (dash-blue) showing the agreement between experimental result and theory. **(b)** Broadening of coercive field of Permalloy in the heterostructure Pt (5 nm)/Permalloy (Py) (4nm)/Cr_2O_3 (30 nm)/V_2O_3/Al_2O_3 at low temperatures. **(c)** Exchange bias field (top panel) and coercive field (bottom panel) as a function of temperature for Pt $(5\,nm)$/Permalloy (Py) $(4\,nm)/Cr_2O_3$ $(30\,nm)/V_2O_3/Al_2O_3$ and control sample Pt $(5\,nm)$/Py $(4\,nm)/Al_2O_3$ heterostructures. The control data of permalloy shows both $\pm 5000\,Oe$ cooling field scans. Adapted from [21]. . . . 55

4.5.1 **(a)** Raw anomalous Hall signals without any correction for each configuration shows error coming from asymmetric contacts. **(b)** Raw anomalous Hall signals at different temperatures shows temperature drifts. **(c)** After signal correction using spinning current offset, the offset due to instrument uncertainty. 56

4.5.2 **(a)** Anomalous Hall signal as a function of temperature, raw data. **(b)** Anomalous Hall signal as a function of temperature, shifted data to remove error from instrument uncertainty. 56

5.1.1 **(a)** X-ray diffraction of Boron-doped Cr_2O_3 grown on (0001) Al_2O_3 and V_2O_3 electrode, in comparison with pure Cr_2O_3 grown on bare (0001) Al_2O_3. **(b)** Boron detection of Boron doped Cr_2O_3 grown on Al_2O_3 using XPS. **(c)** Dielectric behaviour of Boron-doped Cr_2O_3 grown on V_2O_3 electrode, the estimated thickness is in the range of ~ 55 to $60\,nm$. 60

5.1.2 **(a)** Density functional theory calculation of density of state (DOS) for B impurity in Cr_2O_3, with the normal number of electron (top panel) and in the Slater transition state (bottom panel). The dashed line is Fermi level, while the black line is the total DOS and the blue shaded area is the local DOS for Boron impurity. Printed with permission from [24]. **(b)** Electrical behaviour of $200\,nm$ Boron-doped thin film, adapted from [25]. 61

5.2.1 Isothermal switching of $200\,nm$ thick Cr_2O_3 film showing switching characteristics at certain temperature. Adapted from [14]. 62

List of Tables

2.1.1 Some fundamental difference in deposition parameters of certain growth techniques, adapted from [26]. 11

3.1.1 Cation-anion distances in Å (adapted from [27]) 25

3.2.1 Nominal in-plane strain values for each substrate. 29

3.3.1 Thickness of TmIG films estimated from X-ray reflectometry. 30

3.3.2 Lattice constants of film and substrate, calculated from different X-ray diffraction techniques, unit in Å, adapted from [21]. 31

4.1.1 A list of some materials which possess magnetoelectric effect. 42

List of Abbreviations

CMOS Complementary metal-oxide-semiconductor

PLD pulsed laser deposition

PPMS Physical Property Measurement System

RMS root mean square

RSM Reciprocal space mapping

SHG second harmonic generation

TmIG $Tm_3Fe_5O_{12}$

VSM vibrating sample magnetometer

YIG $Y_3Fe_5O_{12}$

Abstract

Modern electronics industry has been focusing on the development of semiconductor-based hardware, with tremendous effort being invested in transistor scaling technology. While worldwide energy consumption is predicted to increase up to 21% by 2030 with ever-growing demands in computing power and speed, the scaling in power consumption in semiconductor-based devices has come to a halt. Spintronic technology, which relies on the use of electron spins in magnetic materials, has the potential to alleviate this problem. Magnetization switching offers the benefit of nonvolatility, low operation energy, and fast performance. Notwithstanding, the miniaturization capabilities in these magnetic systems are often overlooked. Despite the recession in voltage scaling, the semiconductor industry has set a standard for desired transistor size, which currently reaches 3 nanometers in dimensions. At the same time, materials performance in room temperature magnetic systems are primarily focused on hundreds of nanometers scale. Size scaling in spintronics, therefore, is vital towards future technological adoptions. This thesis explores the size scaling capacity of two classes of thin-film magnetic oxides with perpendicular magnetic anisotropy, a configuration that is promising for high-density spintronics-based electronics. This work addresses prior challenges resulting from lattice strain and epitaxy for improved performance at scale.

Spin current switching of magnetism in insulating magnets has the advantage of simple device geometry and isolation of read and write operations (low leakage current). At nanoscale limits, however, insulating ferro/ferrimagnetic oxides experience instability caused by thermal fluctuations. To overcome this problem, the anisotropy energy, the energy needed to switch its magnetization direction and scales with the volume of the magnet, is required

to stay above $42k_BT$, which is the industry standard for ten years of stability of recorded information. At the same time, minimizing the anisotropy energy is the key to a low switching current threshold. The direct relation between anisotropy energy and lattice distortion in a crystal opens a means to tune materials property effectively to meet both requirements. The effect of strain modulation is studied on epitaxially grown $Tm_3Fe_5O_{12}$, an insulating ferrimagnet with perpendicular magnetic anisotropy. Through deposition control and systematic variation of in-plane strain using different substrates, the magnetic anisotropy field is tuned by a factor of 14, and the magnetoelastic anisotropy constant is two times larger than the bulk value. I have demonstrated the tuning window for anisotropy energy that pushes the size limit closer to the desired value.

Electric field switching of magnetization is the most desirable form of operation for future electronic devices due to the elimination of electric current. Among potential candidates that exhibit the ability to manipulate magnetism with an electric field, Cr_2O_3 is among the promising candidates that are single-phase, possess perpendicular anisotropy, and function at room temperature. Despite being one of the most studied materials, the technological challenge in thickness scaling has made Cr_2O_3 an unattractive alternate solution in the semiconductor industry. Considerably large leakage current and low breakdown voltage in crystallographically twinned Cr_2O_3 grown on metallic electrodes, which could only be mitigated with film thicknesses of several hundreds of nanometers, hamper its further development in energy-efficient electronics. By taking advantage of isostructural growth with an oxide electrode and minimal lattice strain, I have achieved a high-quality single crystal thin film of sub-100 nm thickness. The films exhibit not only bulk-like resistivity and significantly improved breakdown voltage but also magnetoelectric symmetry at room temperature for thicknesses as low as 30 nm. For the first time, without elemental doping, I have shown an increase in operating temperature for thin-film Cr_2O_3 compared to the room temperature limit of bulk crystal, which is not often the case in magnetic materials due to finite size limit. This result has transformed Cr_2O_3 from being a mere interesting study subject to an auspicious system for future practical applications.

Chapter 1

Perpendicular Magnetic Insulators Towards Energy Efficient Electronics

Complementary metal-oxide-semiconductor (CMOS) transistors, the dominant semiconductor technology for the past 20 years, utilizes semiconductor heterojunctions to manipulate the flow of electron charge to operate memory and logic devices.[28] Since the prediction made by Gordon Moore in 1965 [29], which stated that the number of transistors in an integrated circuit would double every year, tremendous efforts have been invested in transistor scaling technology to meet the increasing demands in computing power and speed without sacrificing size. Throughout the years, the miniaturization has reached a few nanometers in dimensions by drastic improvement in mobility, gate dielectric, and device designs while maintaining the use of semiconductors as the core materials.[28] The scaling in power consumption and frequency, however, have come to a halt. Governed by the Boltzmann limit[1], the power consumption by a circuit is reducing with a slower speed compared to Moore's law (Figure 1.0.1) [1], while the global energy consumption is predicted to increase by 8 to 21% by 2030 [30]. To overcome this problem, the search for alternative material classes and switching methods got underway.[31] Among potential candidates, magnetic materials utilizing the electron spin offer significant advantages such as non-volatility, low energy dissipation.[32]

[1] At room temperature, every change in a current by a factor of 10 requires $60\,mV$ at minimum.

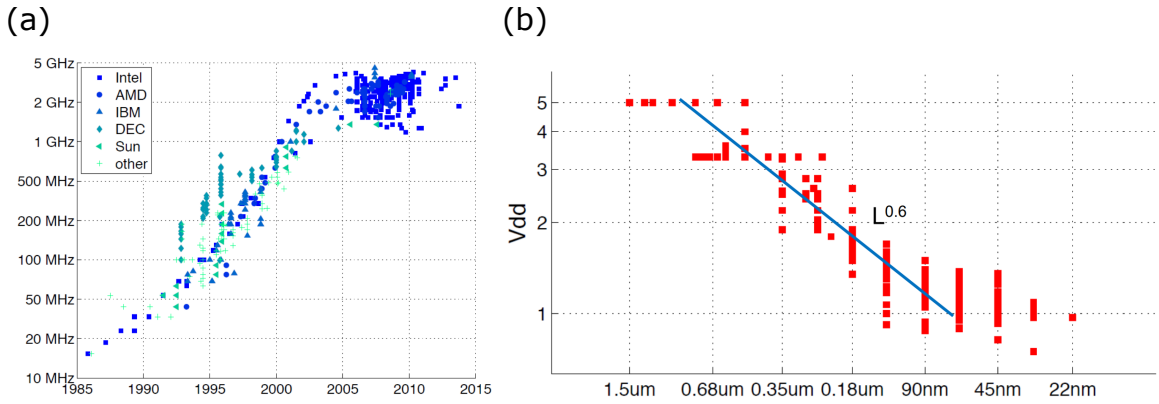

Figure 1.0.1: **(a)** Frequency scaling progress over the year. **(b)** Apply voltage scaling with device size. Images reprinted with permission from [1].

Materials that exhibit magnetic order with a perpendicular spin configuration are of particular interest due to their stable states when being integrated together in a circuit, and therefore allow a denser packing of devices (Figure 1.0.2). Two well-established switching methods (current switching and electric field switching of magnetization) will be discussed below, along with two promising materials for demonstrating the challenges in device scaling.

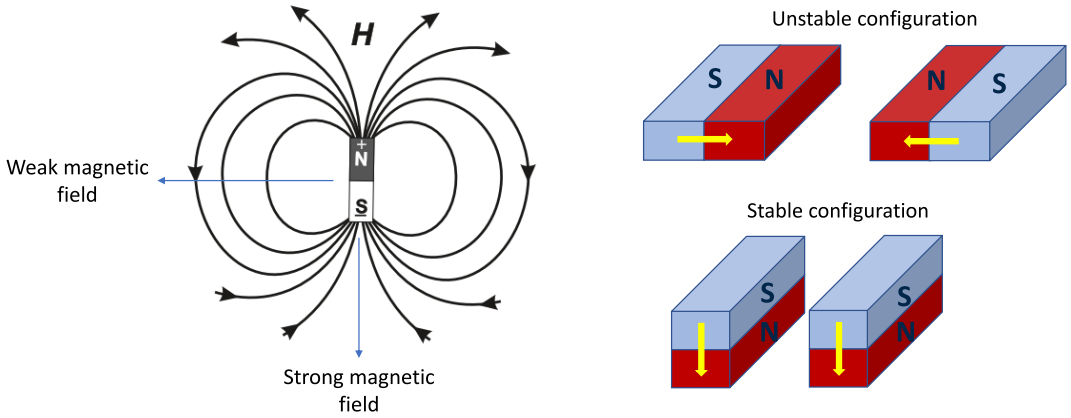

Figure 1.0.2: Stable state of magnetic memory cells is in perpendicular configuration, adapted from [2].

1.1 Spin current switching of magnetic orientation in magnetic insulators

Ferromagnetic materials exhibit a nonlinear response of its magnetization to magnetic field as described in Figure 1.1.1(a). The required magnetic field needed to saturate a crystal depends on the angle between the applied field and the crystal axes. The term *magnetic anisotropy energy* K_u is defined as the energy required to rotate the magnetization from an easy axis (an axis in a crystal along which the smallest magnetic field is needed to saturate the magnetization) to a hard axis (an axis in a crystal along which the largest magnetic field is needed to saturate the magnetization).[2]

Injection of a spin-polarized current can manipulate magnetization of a ferromagnet through angular momentum transfer, as a more realistic, efficient alternative to a magnetic field.[33] Under the applied torque from the spin current, the magnetization $\mathbf{m}$ in a ferromagnetic layer experiences a precessional motion (Figure 1.1.1(d)) that can be described by Landau-Lifshitz-Gilbert (LLG) equation:[33]

$$\frac{d\mathbf{m}}{dt} = \gamma[\mathbf{m} \times \mathbf{H}] + \frac{\alpha}{m}\left[m \times \frac{d\mathbf{m}}{dt}\right] \tag{1.1.0.1}$$

with constant α being damping parameter. $\mathbf{H}$ is effective magnetic field that includes contributions from:

$$H_{eff} = H_{external} + H_{exchange} + H_{anisotropy} + H_{demagnetization} + ... \tag{1.1.0.2}$$

Solving the LLG equation, the critical switching charge current, $J_{c,write}$, by spin-orbit torque with injection of an in-plane polarized spin current, can be derived as:

$$J_{c,write}^{IP} = \frac{2e}{\hbar}\mu_o M_s H_K t\alpha \left(1 + \frac{H_D}{H_K}\right)\frac{1}{\theta_{SH}} \tag{1.1.0.3}$$

t, M_s, e, $\hbar$ and θ_{SH} are film thickness, saturation magnetization, elementary charge, Planck

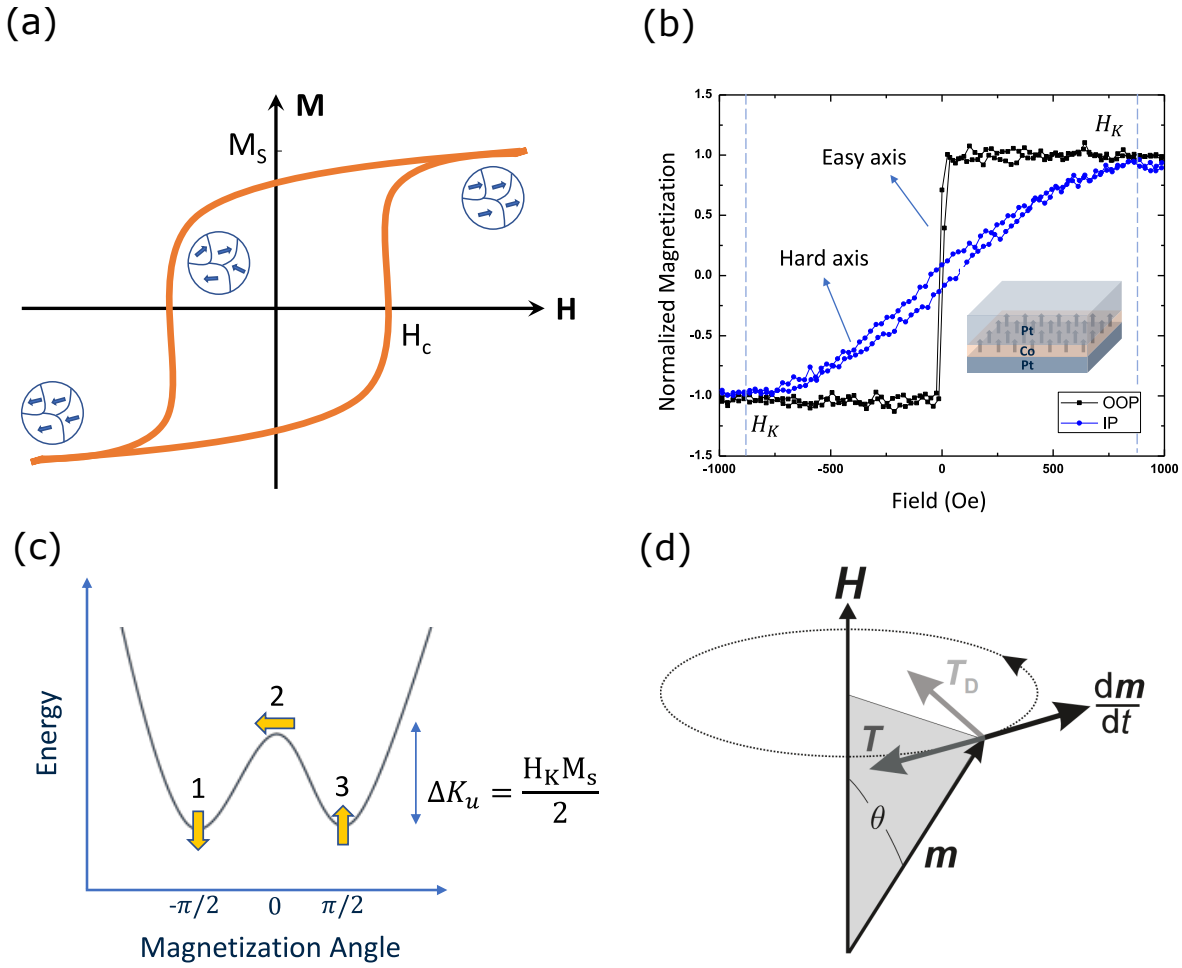

Figure 1.1.1: **(a)** Hysteresis of a ferromagnet, showing the definitions of saturation magnetization M_s and coercive field H_c, adapted from [3]. **(b)** Out-of-plane (OOP) and in-plane (IP) magnetometery of a perpendicular magnet (Pt/Co/Pt), stating the definition of anisotropy field H_K, which is the field needed to rotate the magnetization from easy axis to hard axis. **(c)** Anisotropy energy explanation. **(d)** Torques acting on magnetization **m** cause a precessional motion, adapted from [2].

constant and spin Hall angle[2]. Anisotropy field H_K is related to anisotropy energy through $H_K = \frac{2\Delta K_u}{M_s}$. Material parameter α affects the motion of the magnetization vector.[34] Typical value for α in metallic ferromagnets lies in 10^{-3} regime while it can reach 10^{-4} to 10^{-5} for insulating ferromagnets.[35] Amplitude of demagnetizing field H_D for an in-plane

[2]The efficiency of spin to charge conversion

magnet is estimated as:[2]

$$H_D^{IP} = 4\pi M_s \tag{1.1.0.4}$$

while for an out-of-plane magnet:

$$H_D^{OOP} = N_D M_s \tag{1.1.0.5}$$

N_D is demagnetizing factor ($N_D = 1$ for perpendicularly magnetized film).[2] Under the assumption that other parameters are more or less similar, with sample size being $5 \times 5\, mm^2$, for an in-plane magnet permalloy ($M_s = 800\, emu/cc$, $H_K = 10\, Oe$)[36, 37] and an out-of-plane magnet Cobalt ($M_s = 1400\, emu/cc$, $H_K = 1000\, Oe$) (Figure 1.1.1(b)), the current switching ratio between them is estimated to be:

$$\frac{J_{c,write}^{IP}}{J_{c,write}^{OOP}} = \frac{M_s^{IP}}{M_s^{OOP}} \frac{H_K^{IP} + H_D^{IP}}{H_K^{OOP} + H_D^{OOP}} = \frac{800}{1400} \frac{10 + 4\pi 800}{1000 + 1400} \approx 2.39 \tag{1.1.0.6}$$

For an all perpendicular geometry (perpendicular magnet and perpendicularly polarized spin current), the switching current is quantified as:[38]

$$J_{c,write}^{OOP} = \frac{2e}{\hbar} \mu_o M_s H_K t \alpha \frac{1}{\theta_{SH}} \tag{1.1.0.7}$$

Unlike ferromagnets, ferrimagnetic[3] insulators (FI) have lower magnetization M_s and damping constant α, which would require lower switching current threshold. Among them, $Tm_3Fe_5O_{12}$ (TmIG) belongs to the group of magnetic garnet that recently attracts considerable attention due to its high operating temperature ($560\, K$)[39] and the achievement of high quality thin films with perpendicular magnetization through various deposition techniques[39, 40, 41] by utilizing epitaxy and strain (detailed discussion continues in **Chapter 3**). These advancements in material quality have stimulated the realization of efficient

[3]In Ferrimagnets, there are two anti-parallel sublattices with different magnetization magnitude, therefore, the net magnetization is non-zero but much smaller than a ferromagnet.[2]

current-driven magnetization control.[42, 32] Unlike conducting ferromagnets through which both charge and spin current can propagate, only spin current can pump through the surface of the FI to generate spin-torque for magnetic modulation, which significantly reduces heat dissipation. Current-driven control of magnetization in insulating garnets offers the benefit of device simplification and avoids the problem of leakage current at ultrathin limit ([43]). From equation (1.1.0.7), it is necessary to reduce the anisotropy field for lower switching threshold. When considering thermal fluctuations at nanoscale limit, reduction of H_K compromises device stability. A standard device stability condition is defined as:

$$\frac{M_s V H_K}{2} = 42 k_B T \tag{1.1.0.8}$$

$42k_BT$ is the industry standard number for 10 years of stability of recorded information.[44] With anisotropy field $H_K = 600\, Oe$, saturation magnetization $M_s = 94\, emu/cc$, smallest device can be manufactured that will maintain the stability condition is $64 \times 64 nm^2$, which is far above the currently achieved size in semiconductor. This emphasizes the need to understand and quantify the evolution of H_K with strain to maximize the switching performance at scale.

1.2 Electric field control of magnetism

Magnetoelectric and multiferroic materials/composites possess more than one (anti)ferroic order. The coexistence and coupling between different orderings in the same phase allow one property to be manipulated by the associate/related field of the other. Notably, systems that exhibit both magnetic and electric orderings may permit the use of electric field to control its magnetism, which paves the way for ultra-low switching energy. Energy required in electric field switching is estimated to be 10^4 times lower than in spin current switching of magnetization.[31, 40, 45] When considering device scaling, quality of materials at thin-film limit needs to be evaluated. The electric field required for magnetization switching increases along with a decrease in working temperature due to leakage current [4] and size effects [46].

Chromium oxide (Cr_2O_3)

Antiferromagnetic Cr_2O_3 is one of the few materials exhibiting magnetoelectricity at room temperature ($308\,K$ for bulk crystal [22]), which paves the way to electric field control of magnetization for ultra-low energy dissipation. Its spin structure being parallel to [0001] direction combined with an uncompensated magnetic layer at the (0001) surface leads to exotic proximity effects when comes in contact with a wide range of magnetic systems such as high spin orbit coupling metals[47, 48], van der Waals materials, or perpendicular ferromagnetic heterostructures [22].

Since the demonstration of isothermal magnetoelectric switching of bulk crystal Cr_2O_3 by He *et al.* in 2010 [22], considerable efforts have been put on high-quality thin film fabrication for device miniaturizing and therefore technological and commercial adoption. High quality Cr_2O_3 can be grown on sapphire substrate with relatively ease. The problem lies in the buffer electrode needed for electric field application. With its hexagonal crystal structure, the existence of twin crystallographic domains in Cr_2O_3 thin film on an electrode seriously compromises its dielectric properties, which reduces effective electric field and increases energy dissipation from leakage current [4]. Experiments have shown that the conducting nature of twin Cr_2O_3 comes from its twin domain walls (Figure 1.2.1), which can be overcome by increasing the film thickness. [4, 5] This unideal solution raises the switching voltage significantly ($\approx 80\,V$ for $500\,nm$ film) making Cr_2O_3 an unattractive alternate solution for CMOS technology.

This dissertation will focus on addressing fabrication challenges of above two materials that hamper their capability for device miniaturization. **Chapter 2** reviews experimental methods employed in these studies. **Chapter 3** focuses on strain modulation of TmIG for a stable device at room temperature. **Chapter 4** details the challenge in growing Cr_2O_3 on different electrodes to achieve single crystal film that retains its bulk properties at ultra-thin limit. **Chapter 5** will present preliminary results that support future directions for further developments of Cr_2O_3 thin film towards a low-energy consumption and high operating temperature spintronic devices.

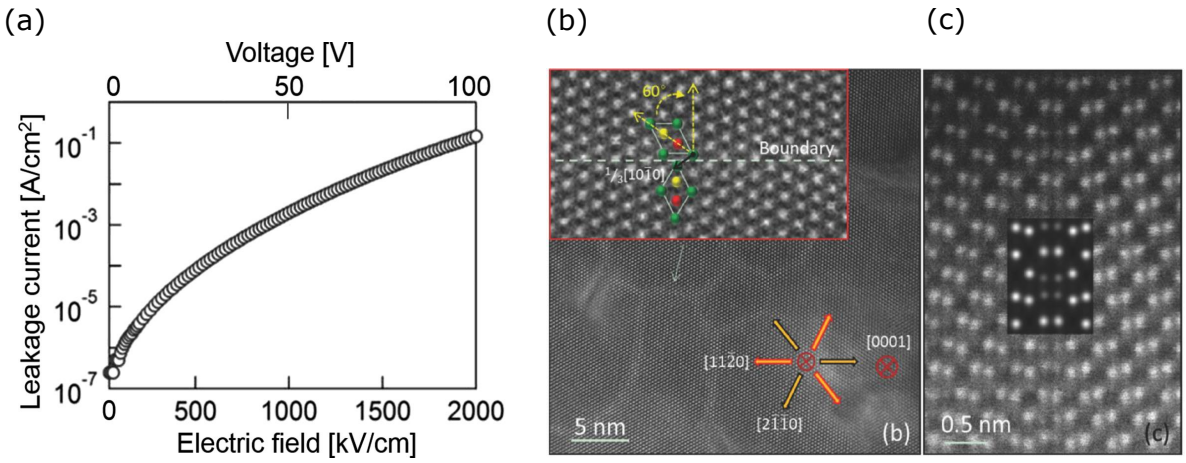

Figure 1.2.1: **(a)** Leakage current of $500\,nm$ thick Cr_2O_3, reprinted with permission from [4]. High angular annular dark field scanning transmission electron microscopy of **(b)** plan view along [0001] of Cr_2O_3 on Al_2O_3, showing crystallographic domains (the inset shows higher resolution image), and **(c)** domain boundary atomic structure along $[11\bar{2}0]$, reprinted with permission from [5].

Chapter 2

Experimental Methods

2.1 Pulsed Laser Deposition

Thin film magnetic oxides, conducting electrodes, and magnetic metal layers are fabricated by pulsed laser deposition (PLD). A high, instantaneous power laser source (COMPex 205, KrF laser, 248 nm wavelength, 25 ns pulse duration, average power of 50 W, maximum energy per pulse is approximately 640 mJ) is directed and focused on a dense target inside a vacuum chamber (Figure 2.1.1 (a)). When laser photons hit the solid surface and are absorbed, electromagnetic energy transforms into an electronic excitation and then thermal, chemical, even mechanical energy that causes ablation.[26] Species ablated from the targets will form a plasma plume and is directed towards a substrate under a heater within the chamber. Elemental transfer is nominally stoichiometric with the target, but selective desorption of adatoms on the substrate surface can lead to composition differences .[26] By varying the growth parameters such as:

- Laser fluence (laser energy/laser spot size)
- Laser pulse repetition rate
- Substrate temperature (from room temperature to 950 ^oC)
- Chamber pressure (from 5×10^{-8} Torr to 2.5 Torr)

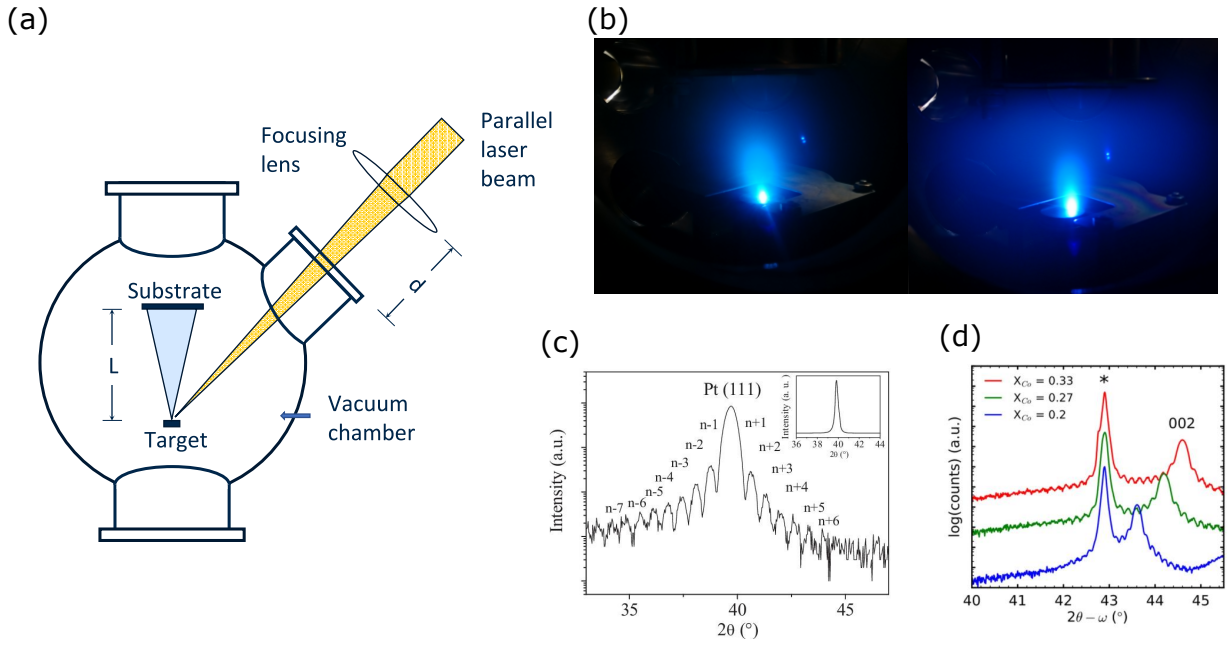

Figure 2.1.1: **(a)** Schematic of pulsed laser deposition. **(b)** Plasma plumes at different background gas pressures. High resolution X-ray diffraction showing Laue oscillation of **(c)** Pt deposited on YSZ (111) with Ti buffer layer, reprinted with permission from [6], and **(d)** Entropy-stabilized oxide deposited on MgO (001) $(Mg_{0.25(1-x)}Co_xNi_{0.25(1-x)}Cu_{0.25(1-x)}Zn_{0.25(1-x)})O$, adapted from [7], indicates highly crystalline and smooth thin films grown by PLD.

- Reactive gas (O_2), non-reactive gas (Ar, N_2)

PLD is capable of producing high quality thin films (highly crystalline, smooth surface) and metals (Figure 2.1.1 (c), (d)).[7, 6] This makes fabrication of complex oxide heterostructures with metals feasible, as proposed here, particularly with metals that have high melting or vaporization temperatures.[49] Some fundamental signatures in growth parameters of PLD are listed in table 2.1.1, which suggests its advantages over certain techniques in achieving desired thin film qualities.

Growth modes of thin films

Comprehensive studies in thin film growth using PLD can be found in different textbooks with great details and examples.[26, 50] This section will briefly discuss qualitative tuning

Table 2.1.1: Some fundamental difference in deposition parameters of certain growth techniques, adapted from [26].

Method	Species kinetic energy (eV)	Vacuum requirement	Typical deposition rate (Å/s)	> 10 mTorr Reactive gas
CVD [1]	0.1	HV [3]	20	Yes
MOCVD [2]	0.1	UHV [4]	10	Yes
MBE [5]	0.1	UHV	1	No
PLD	1 - 1000	HV	1	Yes
Sputter	1 - 1000	HV	10	No

[1,2] (Metalorganic) Chemical Vapor Deposition [3] High vacuum

[4] Ultra-high vacuum [5] Molecular beam epitaxy

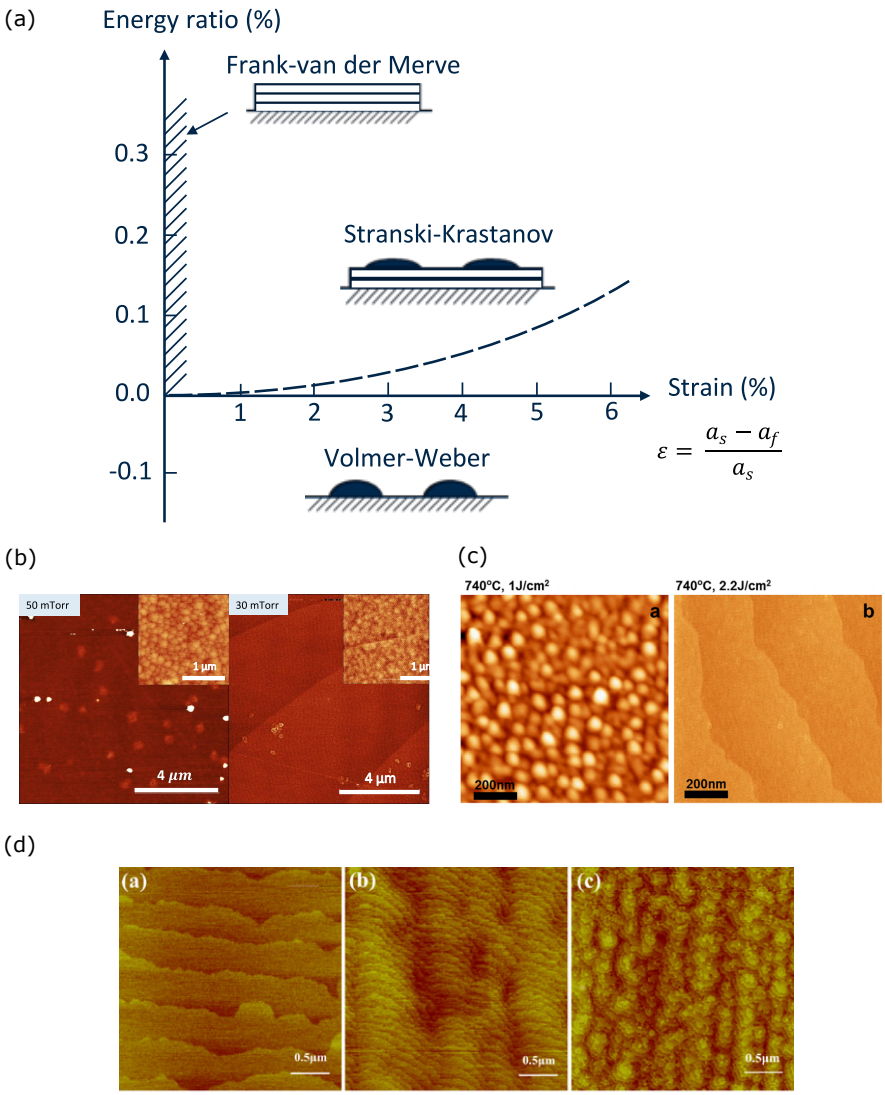

Figure 2.1.2: **(a)** Growth modes in thin film, energy ratio is defined as $\Phi_{fs}/\Phi_{ss} - 1$, with Φ is interatomic potential of film-substrate or substrate-substrate, adapted from [8, 9]. **(b)** Topography changes with oxygen pressure in Cr_2O_3 grown on (001) Al_2O_3. **(c)** $La_{0.7}Sr_{0.3}MnO_3$ grown on (001) $SrTiO_3$ changes its growth mode with laser fluence, printed with permission from [10]. **(d)** Topography of $SrRuO_3$ grown on (100) $SrTiO_3$ at different temperatures (from left to right: 688, 642, 592^oC), adapted from [11].

of growth parameters to achieve better film quality. In thin film fabrication, there are three different growth modes: Frank-van der Merwe (FM) (layer-by-layer growth), Volmer-Weber (VW) (island growth) and Stranski-Krastinov (SK) (intermediate mode). The FM mode is

the most desirable since it gives the highest surface quality but not always achievable for every material system. The condition for FM growth mode can be simplified as:

$$\gamma_s \geq \gamma_f + \gamma_{sf} \tag{2.1.0.1}$$

with γ_s, γ_f, and γ_{sf} are surface energy of substrate, film, and interface between film and substrate.[9] Therefore, FM growth mode is favorable for substrate with high surface energy, film with low surface energy and strong film-substrate bonding.[26] FM mode can also be achieved with approximately zero misfit between substrate and film (Figure 2.1.2(a)).[9] These favorable conditions, however, are hardly met while attempting to create novel structures to meet application needs.

Layer-by-layer growth is essentially the nucleation of two-dimensional, one-monolayer-thick islands. Each layer will fully grow before clusters start to form for the next layer. High nucleation density tends to promote the complete growth of full monolayers, which can be tuned mainly by deposition rate and substrate temperature. High laser fluence intensifies the cluster formation that would promote the layer-by-layer growth mode (Figure 2.1.2(c)). At certain fluence threshold, the appearance of particulates takes place and therefore increasing fluence further is no longer an option. At the same time, adjusting substrate temperature can produce similar effect. Substrate temperature influences adatom diffusion which affects nucleation rate. On the other hand, an increased substrate temperature would increase adatom mobility to form layer by layer (Figure 2.1.2(d)). The interplay between laser fluence, species energy and substrate temperature permits the growth of high quality thin film at low temperature that is favorable for the protection of underlying layers. Lastly, background gas pressure is expected to be capable of modifying surface free energies of substrate and film, and therefore can change the film growth mode. This, however, is merely a speculation, for the effect is only significant at very high pressure, at which the benefit of high kinetic energy species is often lost, along with the significant increase in particulates formation.[26] Lower background gas pressure is usually associated with smoother film (Figure 2.1.2(b)), however, one should keep in mind that certain materials require high background pressure

of reactive gas to reach desirable qualities (such as room temperature ferromagnetism in $La_{0.7}Sr_{0.3}MnO_3$ [51] or perpendicular magnetization in ferrimagnets [52]).

2.2 X-ray diffraction

Symmetric $2\theta - \omega$ scan

Bragg's condition states that the relationship between interplanar spacing of plane (hkl), diffraction angle θ and X-ray wavelength λ can be expressed as:

$$2d_{hkl}sin(\theta) = n\lambda \tag{2.2.0.1}$$

n is diffraction order. The interplanar spacing of a cubic with lattice parameter a is:

$$\frac{1}{d_{hkl}^2} = \frac{h^2 + k^2 + l^2}{a^2} \tag{2.2.0.2}$$

and of hexagonal structure with lattice parameter a, c is:

$$\frac{1}{d_{hkl}^2} = \frac{4}{3}\left(\frac{h^2 + hk + k^2}{a^2}\right) + \frac{l^2}{c^2} \tag{2.2.0.3}$$

From the measured diffraction angle, one can calculate the out-of-plane lattice parameter of a thin film and therefore calculate the out-of-plane strain relative to bulk. Figure 2.2.1 describes the geometry of this measurement and sample stage's axes in a typical Rigaku Smartlab system with Cu K-α radiation ($\lambda \approx 1.54$Å).

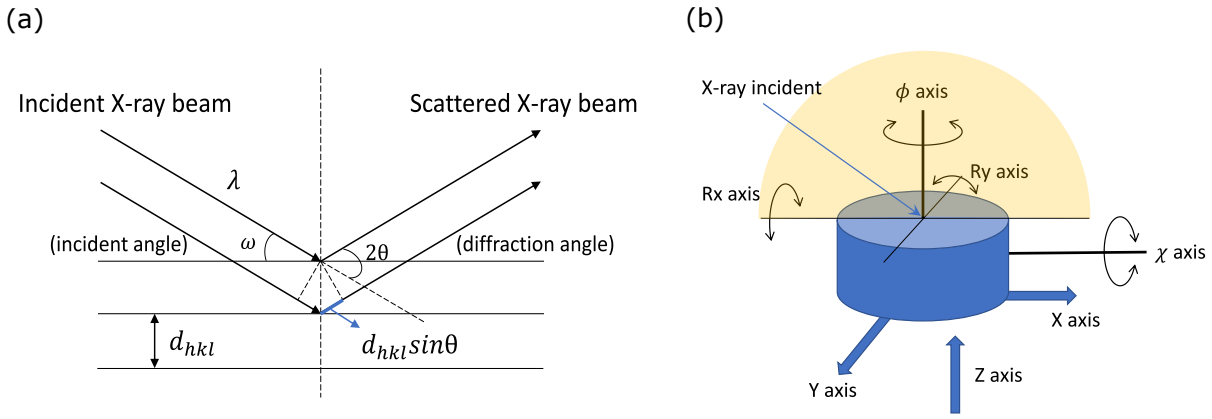

Figure 2.2.1: **(a)** Symmetric X-ray diffraction. **(b)** Standard axes in Rigaku Smartlab diffractometer. Adapted from [12].

X-ray reflectivity [12]

X-ray reflectivity can be used to determine the thickness of films with smooth surface or of layers in heterostructure with smooth interfaces, along with surface roughness and layer density. At grazing angle smaller than a critical value (θ_c), X-ray beam is totally reflected. Critical angle varies between materials and depends vastly on their refractive index or electron density. With Cu K-α for example, critical angle of Platinum (Pt) is approximately 0.5^o while it is roughly 0.3^o to 0.4^o for most oxides. Above this critical angle, the X-rays gradually penetrate the film. If the electron density of each layer is different from each other, the X-rays reflected from each surface/interface will interfere constructively and destructively, resulting in the oscillation pattern observed in the reflectivity data. The oscillation pattern can contain valuable structural information as described in Figure 2.2.2.

Base on the oscillation pattern, the thickness of monolayer film can be estimated using the below relationship:

$$\theta_m^2 = \left(\frac{\lambda}{2d}\right)^2 m^2 + \theta_c^2 \tag{2.2.0.4}$$

with θ_m, m, d are peak position, order of the peak and thickness of the film. This is the case when critical angle of the film is smaller than that of the substrate. Film thickness can then be calculated as:

$$d = \frac{\lambda}{2}\sqrt{\frac{m_2^2 - m_1^2}{\theta_{m2}^2 - \theta_{m1}^2}} \tag{2.2.0.5}$$

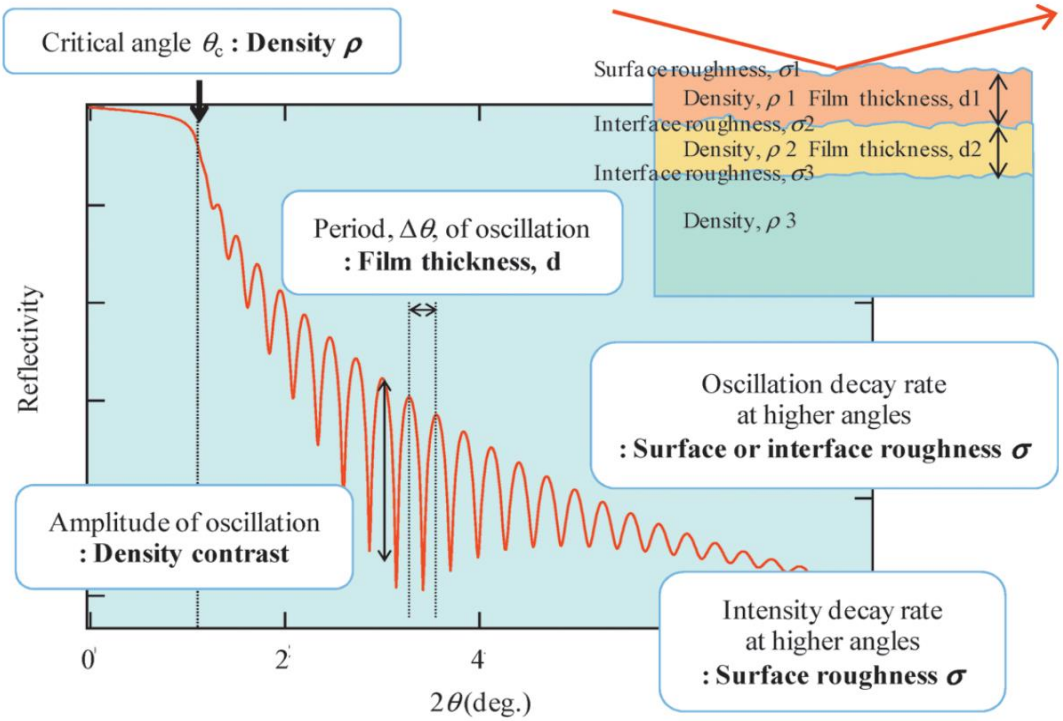

Figure 2.2.2: Information provided by X-ray reflectivity, adapted from [13].

.

Phi (ϕ) scan

Information of the film texture can be acquired using ϕ scan of specific planes that are not parallel to the film surface. After adjusting the goniometer in the Rigaku Smartlab system

to locate the position of the desired plane (e.g. ω and χ, Figure 2.2.1(b)), X-ray diffraction is then scanned across ϕ range while keeping incident beam and detector constant. For a single crystal film, the number of peaks in ϕ scan should be equal to the order of rotational symmetry of the film surface. The case study of (001) Cr_2O_3 grown on different substrates is demonstrated in Figure 2.2.3. Single crystal Cr_2O_3 when grown on (001) plane displays 3-fold symmetry which corresponds to 3 peaks in ϕ scan. The presence of second set of ϕ peak reveals a textured growth with twin domains. The intensity ratio between two sets of ϕ peaks reflects the ratio of each domain in the sample.

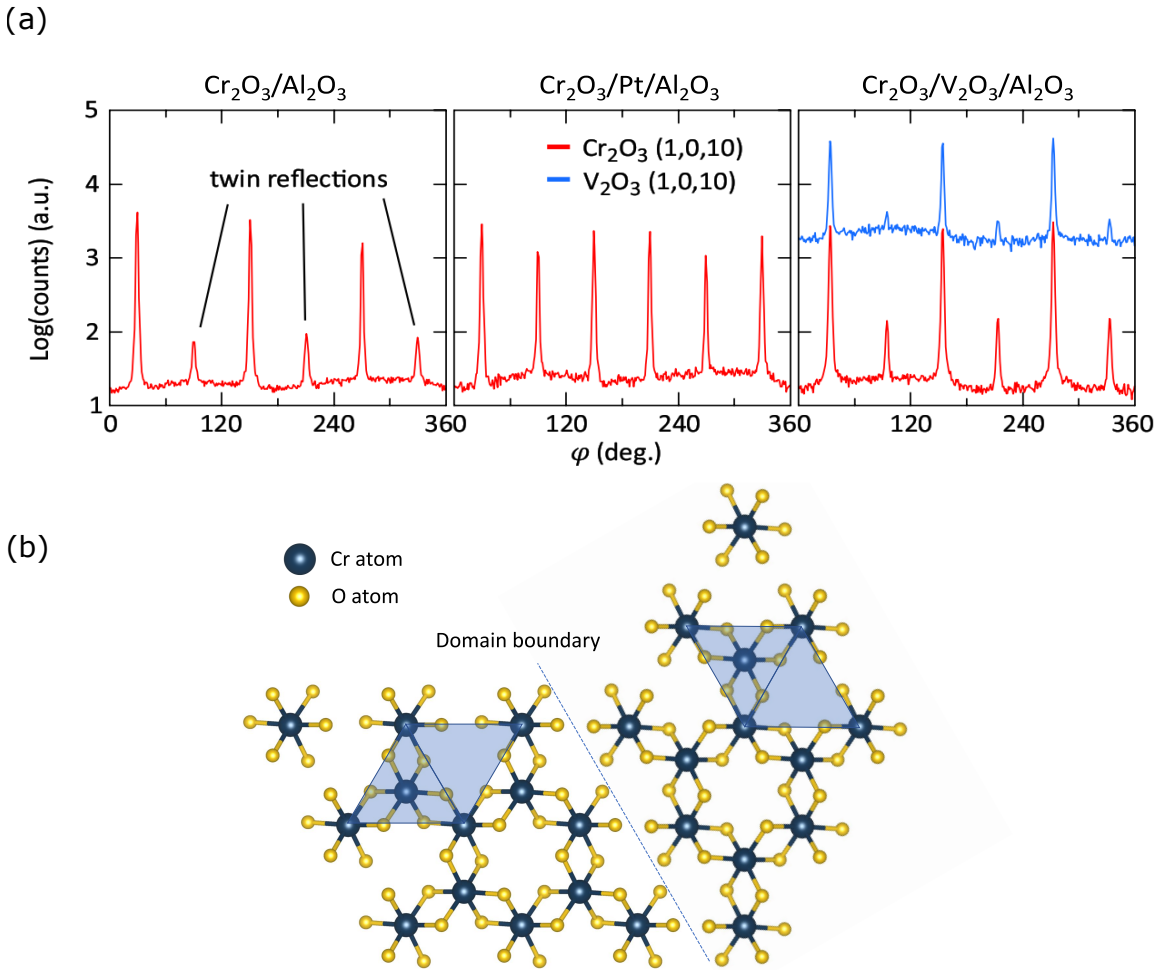

Figure 2.2.3: **(a)** ϕ scan of (1,0,10) plane in thin film Cr_2O_3 grown on different substrates, adapted from [14]. **(b)** 3-fold symmetry of (001) plane in Cr_2O_3 and 60^o rotation of the crystal around [001] axis (Crystal structure was constructed using Vesta software).

Reciprocal space mapping [12]

RSM measures diffraction intensity by scanning both diffraction angle and sample rotational axes. The results are then plotted in reciprocal space and can reflect the strain state of films.[12] The conversion between real space and reciprocal space coordinates is expressed below:

$$Q_x = \frac{1}{\lambda}\left[cos\omega - cos(2\theta - \omega)\right] \tag{2.2.0.6}$$

$$Q_z = \frac{1}{\lambda}\left[sin\omega + sin(2\theta - \omega)\right] \tag{2.2.0.7}$$

The relative position of film and substrate peaks in reciprocal space indicates the degree of lattice matching. The reciprocal point of a fully relaxed lattice will lie in the same line that connects the origin of the reciprocal coordinate and the reciprocal point of the substrate. Projection on to the horizontal axis of the reciprocal point of a fully strained lattice will match with that of the substrate. Correlations between distance in reciprocal space and real space are described in Figure 2.2.4(a).[15] Figure 2.2.4(b) shows an example of fully strained and relaxed $Si_{0.74}Ge_{0.26}$ lattice grown on Si substrate.[16] From Figure 2.2.4(a), in-plane and out-of-plane planar spacing of film and substrate can be derived as:

$$d = \frac{1}{Q} \tag{2.2.0.8}$$

and when combined with equations (2.2.0.2) and (2.2.0.3), the in-plane and out-of-plane lattice parameters can be obtained.

2.3 Vibrating sample magnetometer

Based on Faraday's law of induction, a changing magnetic field creates an electric current that can be detected by a nearby conductor. Therefore, a magnetized, vibrating magnetic sample would create a detectable electric field in a pair pickup coils. From this principle, vibrating

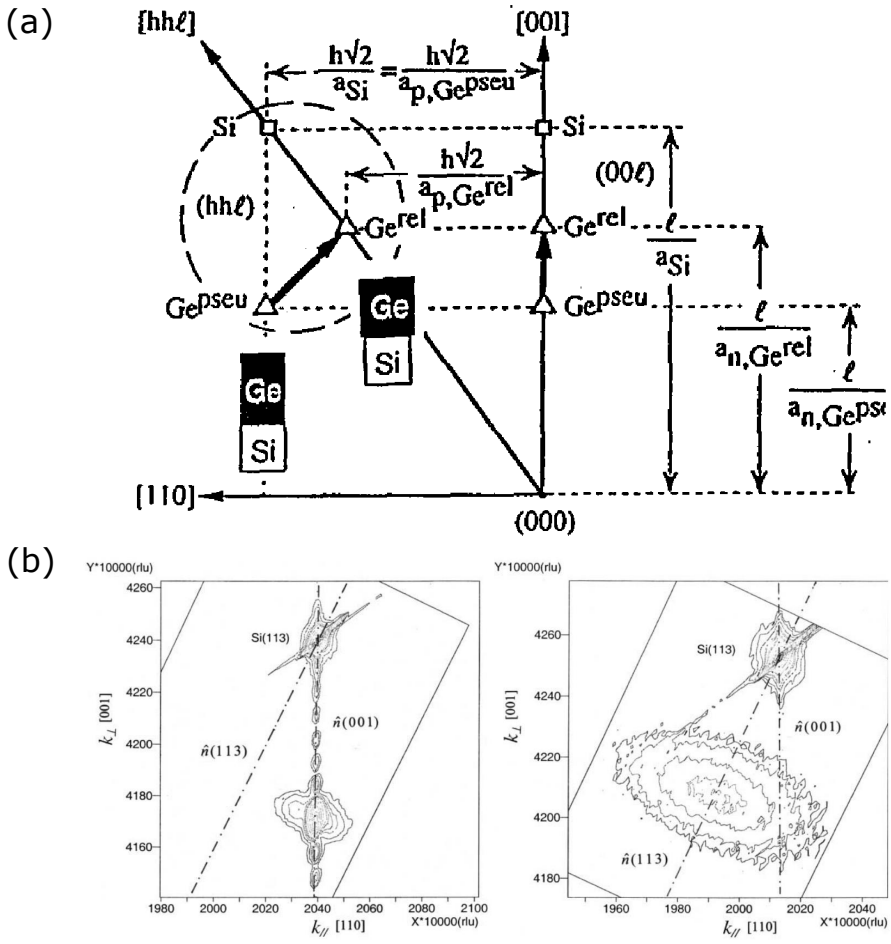

Figure 2.2.4: **(a)** Relations of distances in reciprocal space and real space, demonstrated for Ge film grown on Si (001) substrate, a_p and a_n are in-plane and out-of-plane lattice parameters, adapted from [15]. **(b)** Reciprocal space mapping of (113) plane of $Si_{0.74}Ge_{0.26}$ grown on Si (001) substrate, **left** is fully strained lattice and **right** is partial relaxed lattice, printed with permission from [16].

sample magnetometer (VSM) was built to detect magnetic moment in a magnetic sample with sensitivity level of few micro emu. A typical setup of a VSM is described in Figure 2.3.1. Two systems employed in this thesis are Lakeshore 7400 series (room temperature measurement) and Physical Property Measurement System (PPMS) (with temperature range from 2 K to 400 K).

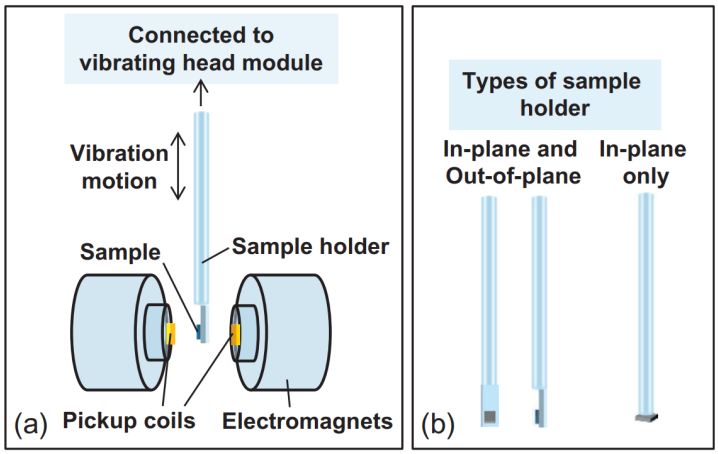

Figure 2.3.1: Typical VSM setup and sample holders for a Lakeshore system, adapted from [17].

2.4 Magneto-transport

Measurement systems

Magneto-transport measurements are performed in PPMS for high field and low temperature scans (above 1 Tesla and below room temperature). For room temperature scan and up to 400 K with low magnetic field, measurements are carried out in our home built transport stick which is installed within the core of the Lakeshore magnet (Figure 2.4.1).

Low signal Hall voltage [18]

Under an applied magnetic field, moving charged particles in a conductor/semiconductor experience Lorentz force that causes their path to curve. Oppositely charged particles experience opposite Lorentz force and therefore accumulate on opposite sides of the material, generating a Hall voltage signal. Hall effect measurements, in general, experience multiple systematic errors that originate from symmetry of the setup, instrument limitation, and intrinsic sources that can be listed below:

- Instrument offset: non-zero voltage signal at zero applied current and vice versa.
- Contact misalignment voltage

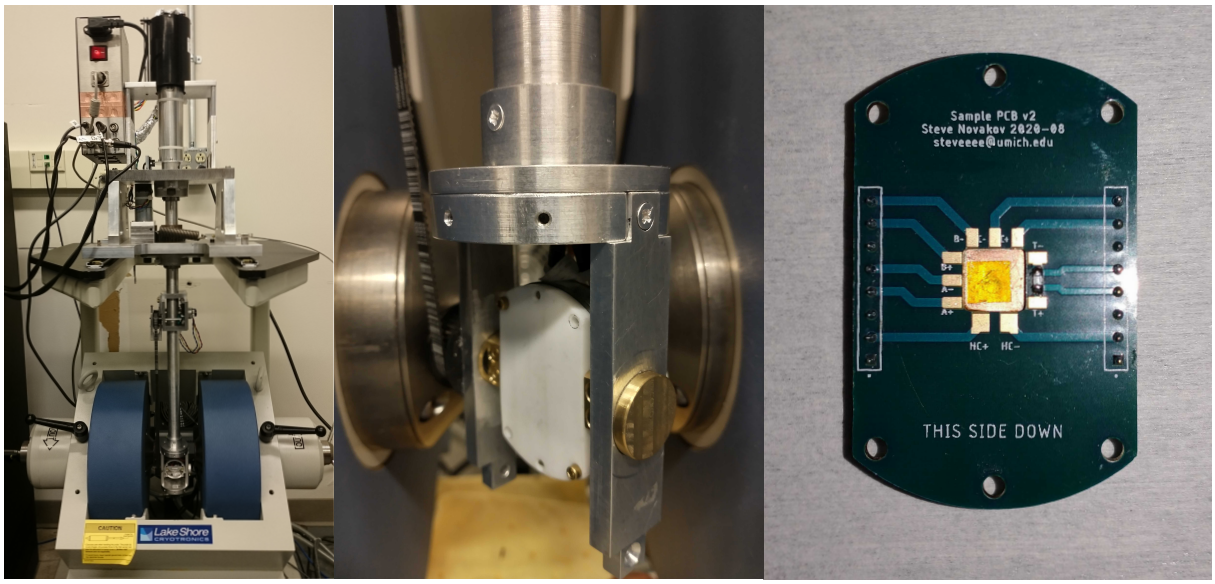

Figure 2.4.1: Transport setup within the Lakeshore magnet.

- Thermoelectric voltage
- Resistance changes as a function of temperature

These errors can effectively be cancelled out by "spinning current offset" method [14, 18]. The principle of this method is briefly explained in Figure 2.4.2(b). The average voltage is the corrected voltage without errors:

$$V_{transverse} \propto \frac{V_{1234} + V_{3412} + V_{2413} + V_{4312}}{4} \tag{2.4.0.1}$$

The spinning current method is performed using a Keithley 2450 sourcemeter as a current source and a Keithley nanovoltmeter 2182A for voltage sensing, in combination with a Keithley 3700A matrix card which performs the rotation of applied current. However, for the Keithley instruments (sourcemeter, nanovoltmeter), one should be aware of the instrument "uncertainty value" that cannot be removed. For the lowest measurement range ($20\,mV$), Keithley 2450 source meter has an uncertainty value of $150\,\mu V$ (Information obtained form Tektronix customer support).

Device fabrication

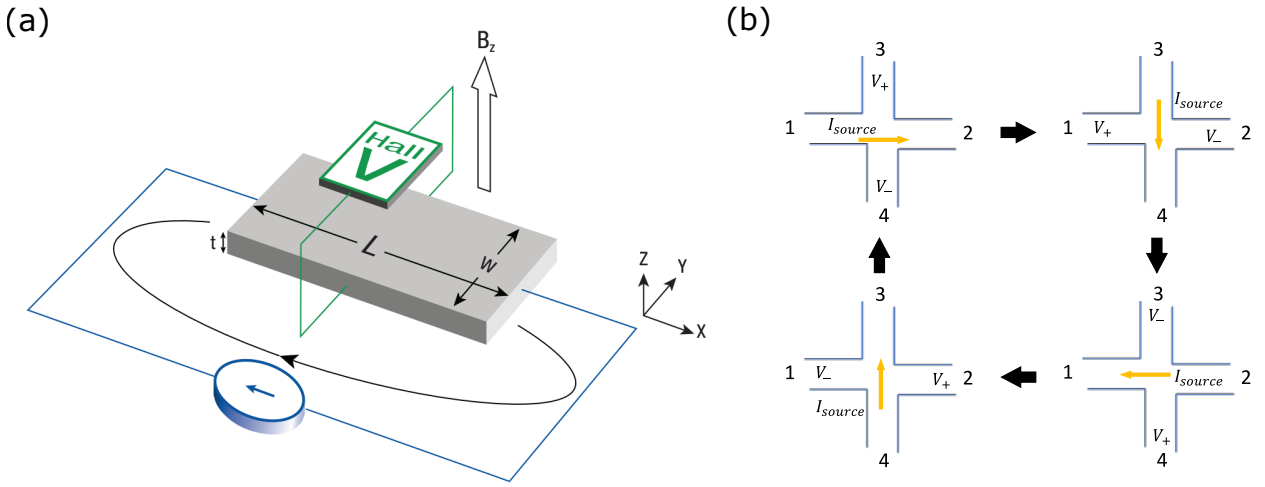

Figure 2.4.2: **(a)** Schematics of Hall measurement, adapted form [18]. **(b)** Spinning current method.

For dielectric characterizations, circular electrode pads are defined using a standard photolithography process. Pt and Ti (as an adhesion layer) are deposited in the PLD chamber in standard condition for metals: room temperature, Ar gas pressure ($10\,mTorr$) and $6\,Hz$ laser deposition rate. For Hall measurement, 2 to $2.5\,nm$ Pt is deposited and then etched into Hall bars by plasma etching. Following standard photolithography process, a insulating layer HfO_2 is use to reduce the contact area between top electrode and Cr_2O_3 film to minimize leakage current. Schematics of device stacks are demonstrated in Figure 2.4.3(a) for circular pads and Figure 2.4.3(b) for Hall measurement.

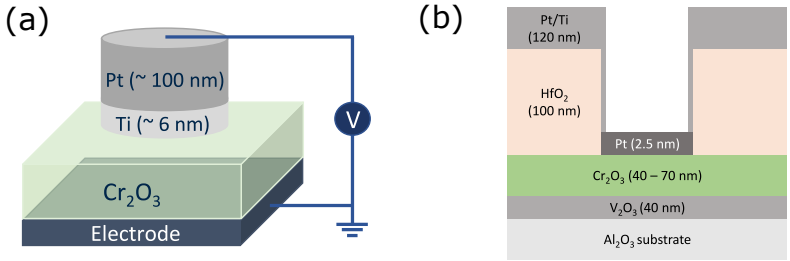

Figure 2.4.3: **(a)** Sample stack for dielectric testing. **(b)** Device stack for Hall measurement.

2.5 Second harmonic generation

In nonlinear optics, second harmonic generation (SHG) refers to the frequency doubling of a light wave passing through crystals of different point group symmetries.[19] The induced second order polarization of emitted light from the crystal is described by:

$$P_i^{2w} = \frac{\epsilon_0}{2}\chi_{ijk}^{(2)} E_j^w E_k^w \tag{2.5.0.1}$$

χ_{ijk} is a susceptibility tensor which reflects the light-matter interaction in different crystal classes. i, j, k are coordinates with respect to crystal axes and $E(w)$ is the electric field component of incident light wave with frequency w.[19] χ_{ijk} is absent in centrosymmetry media and therefore SHG is utilized to detect crystals that lack inversion symmetry, such as crystals with ferroelectric order. Detailed setup of transmission SHG is described in Figure 2.5.1. The incident ultrafast light source has wavelength of $800\,nm$, $40\,fs$ pulse duration and $200\,kHz$ repetition rate. The incident light is focused on to a $20\,\mu m$ spot on the sample with a fluence of $0.25\,mJ/cm^2$.[21]

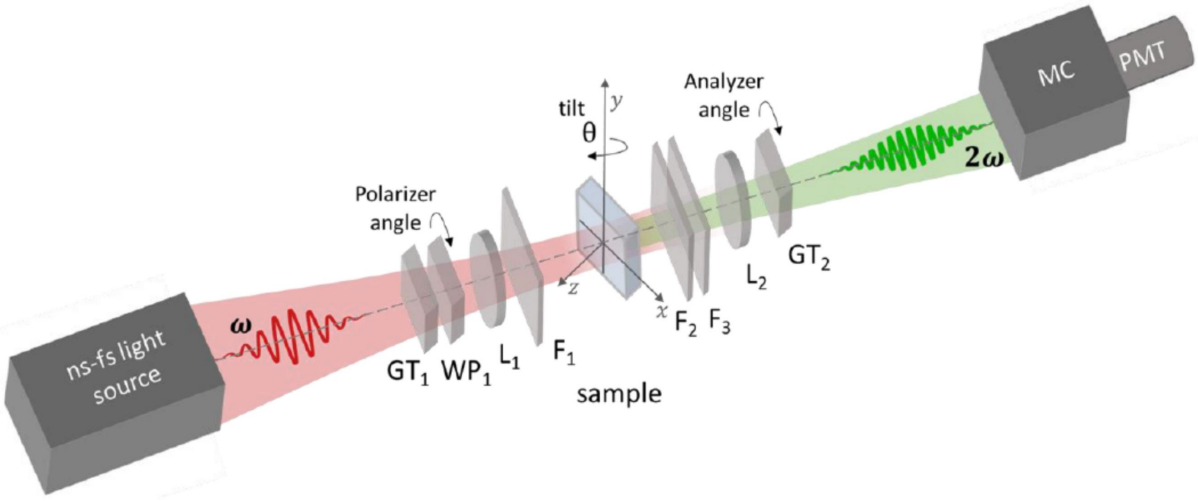

Figure 2.5.1: Typical second harmonic measurement setup in transmission mode. The incident probe beam is linearly polarized with polarization direction defined by the polarizer angle. The polarization direction of the detected second harmonic signal is projected along the analyzer angle. Adapted from [19].

Chapter 3

Strain Tuning in Ferrimagnet $Tm_3Fe_5O_{12}$

3.1 Background: Magnetic anisotropy

Structural description [27]: An explanation for ferrimagnetic order in rare earth iron garnets ($Y_3Fe_5O_{12}$ (YIG), TmIG ...).

Iron garnets (chemical formula $R_3^{3+}Fe_2^{3+}(FeO_4)_3^{-5}$) belong to space group $Ia3d$ [1]. The positions of cations in each unit cell are demonstrated in Figure 3.1.1 below.

These cations are arranged into 3 different sites *c, a, d* corresponding to R_3^{3+}, Fe_2^{3+}, Fe_3. The main contributions to magnetic properties of a iron garnet are Fe-O-Fe $(a-d)$ and Fe-O-R $(c-d)$ interactions. Super-exchange interactions between site a (octahedral) and site d (tetrahedral) creates the ferrimagnetic order with magnetic moment of $5\mu_B$ per formula, which gives $40\mu_B$ per unit cell.

The contribution from c sub-lattices to magnetic behaviour of the system is less obvious. The small difference in Curie temperature of rare earth iron garnets somewhat reveals the insignificance of this contribution, since Curie temperature is related to the number of magnetic interaction. The super-exchange interaction between c sites and d sites are more

[1] This is not strictly true, the ferrimagnetic garnets do not actually belong to cubic space group since it is not possible for a cubic lattice to have a spontaneous polarization, either magnetic or electric. [27]

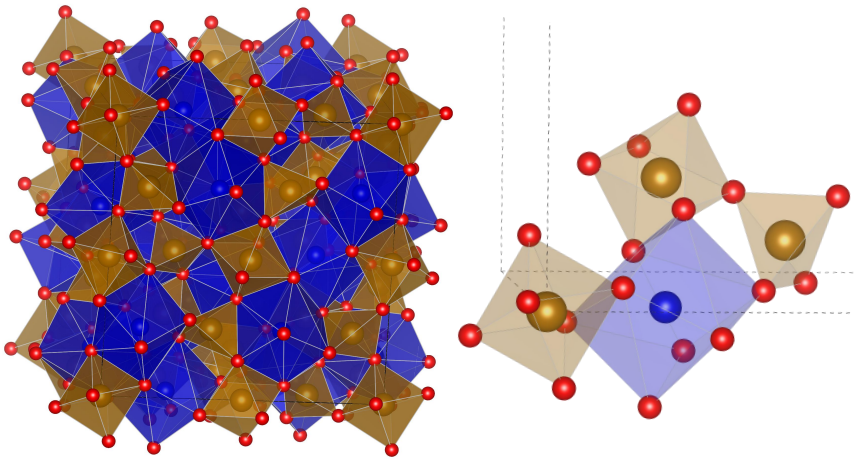

Figure 3.1.1: Left: Polyhedra in one unit cell of $Tm_3Fe_5O_{12}$. **Right**: Zoom-in corner of the unit cell, showing individual Fe^{3+} ions occupy tetrahedral and octahedral sites. Dashed lines represent unit cell (Crystal structure was constructed using Vesta software).

dominant due to the difference in cation-oxide distances (table 3.1.1). In case of TmIG, Tm^{+3} ion has $4f^{12}$ electron configuration which is a paramagnetic ion.

Table 3.1.1: Cation-anion distances in Å (adapted from [27])

	Fe(a)-O	Fe(d)-O	R-O	
Geller and Gilleo	2.01(1)	1.87(1)	2.43(1)	2.37(1)
Batt and Post	2.012(2)	1.881(1)	2.417(3)	2.365(1)

Anisotropy energy calculation [40, 53, 54, 2]

In magnetic materials, anisotropy energy determination is essential to study magnetic structures in materials for applications in such as memory and logic devices.

The total anisotropy energy of a magnetic crystal is expressed below, with K_{mc} to be magnetocrystalline anisotropy, K_{shape} to be shape anisotropy and K_{me} to be magmetoelastic anisotropy:

$$K_u = K_{mc} + K_{shape} + K_{me} \tag{3.1.0.1}$$

For cubic system, the direction cosine components are defined such as:

$$m_1^2 + m_2^2 + m_3^2 = 1$$

Naturally, iron garnets in their crystal forms have a magnetic easy axis [111]. In thin film, the shape anisotropy

For M // [111]: $m_1 = m_2 = m_3 = \frac{1}{\sqrt{3}}$
For M // [11$\bar{2}$]: $m_1 = \frac{1}{\sqrt{6}}$; $m_2 = \frac{1}{\sqrt{6}}$; $m_3 = \frac{-2}{\sqrt{6}}$
For M // [1$\bar{1}$0]: $m_1 = \frac{1}{\sqrt{2}}$; $m_2 = \frac{1}{\sqrt{2}}$; $m_3 = 0$)

Magnetocrystalline anisotropy:

$$K_{mc} = K_1(m_1^2 m_2^2 + m_1^2 m_3^2 + m_2^2 m_3^2);\ K_2 = 0 \,\text{for TmIG}$$

$$[111] : K_{mc} = \frac{K_1}{3}$$
$$[11\bar{2}] : K_{mc} = \frac{K_1}{4}$$
$$[1\bar{1}0] : K_{mc} = \frac{K_1}{4}$$

Magnetoelastic anisotropy:

$$K_{me} = B_1 \left[\left(m_1^2 - \frac{1}{3} \right) \epsilon_{11} + \left(m_2^2 - \frac{1}{3} \right) \epsilon_{22} + \left(m_3^2 - \frac{1}{3} \right) \epsilon_{33} \right] + B_2(m_1 m_2 \epsilon_{12} + m_1 m_3 \epsilon_{13} + m_2 m_3 \epsilon_{23}) \tag{3.1.0.2}$$

$$[111] : K_{me} = \frac{B_2}{3}(\epsilon_{12} + \epsilon_{13} + \epsilon_{23})$$
$$[11\bar{2}] : K_{me} = B_1 \left(-\frac{1}{6}\epsilon_{11} - \frac{1}{6}\epsilon_{22} + \frac{1}{3}\epsilon_{33} \right) + \frac{B_2}{6}(\epsilon_{12} - 2\epsilon_{13} - 2\epsilon_{23})$$
$$[1\bar{1}0] : K_{me} = B_1 \left(\frac{1}{6}\epsilon_{11} + \frac{1}{6}\epsilon_{22} - \frac{1}{3}\epsilon_{33} \right) - \frac{1}{2}\epsilon_{12}$$

Elastic energy:

$$F_{el} = \frac{1}{2}c_{11}(\epsilon_{11}^2 + \epsilon_{22}^2 + \epsilon_{33}^2) + c_{12}(\epsilon_{11}\epsilon_{22} + \epsilon_{11}\epsilon_{33} + \epsilon_{22}\epsilon_{33}) + \frac{1}{2}c_{44}(\epsilon_{12}^2 + \epsilon_{13}^2 + \epsilon_{23}^2) = \frac{3}{4}c_{44}\epsilon_{12}^2 \tag{3.1.0.3}$$

Since $F_{el} = F_{me}$:

$$[111] : K_{me} = B_2\epsilon_{12} = \frac{3}{2}c_{44}\epsilon_{12}^2 \rightarrow B_2 = \frac{3}{2}c_{44}\epsilon_{12}$$

$$11\bar{2} : K_{me} = -\frac{1}{2}B_2\epsilon_{12}$$

$$[1\bar{1}0] : K_{me} = -\frac{1}{2}B_2\epsilon_{12}$$

Since:

$$K_u = K_{mc} + K_{shape} + K_{me}$$

We have:

$$\Delta K_{u[11\bar{2}]} = K_{u[11\bar{2}]} - K_{u[111]} = \Delta K_{mc} + \Delta K_{shape} + \Delta K_{me}]$$

$$\Delta K_{u[1\bar{1}0]} = K_{u[1\bar{1}0]} - K_{u[111]} = \Delta K_{mc} + \Delta K_{shape} + \Delta K_{me}]$$

$$\Delta K_{me} = \Delta K_u - \Delta K_{mc} - \Delta K_{shape}$$

Shear strain:

$$\epsilon_{12} = \frac{1}{2}\left(\frac{\pi}{2} - \beta\right)$$

$$B_2 = -3\lambda_{111}c_{44}$$

We have:

$$\Delta K_{u[11\bar{2}]} = -\frac{K_1}{12} - \frac{1}{2}\mu_o M_s^2 + \frac{9}{4}\lambda_{111}c_{44}\left(\frac{\pi}{2} - \beta\right)$$

$$\Delta K_{u[1\bar{1}0]} = -\frac{K_1}{12} - \frac{1}{2}\mu_o M_s^2 + \frac{9}{4}\lambda_{111}c_{44}\left(\frac{\pi}{2} - \beta\right)$$

The anisotropy for the thin film with (111) plane of cubic system is:

$$\Delta K_u = -\frac{K_1}{12} - \frac{1}{2}\mu_o M_s^2 + \frac{9}{4}\lambda_{111}c_{44}\left(\frac{\pi}{2} - \beta\right) \tag{3.1.0.4}$$

Magnetic anisotropy is related to anisotropy field through:

$$\Delta K_u = \frac{H_k M_s}{2} \tag{3.1.0.5}$$

With equation (3.1.0.5), the magnetic anisotropy can be calculated using anisotropy field obtained from experiments. K_i, B_i are the cubic anisotropy constant and magnetoelastic coefficient respectively. β is the shear distortion angle from cubic geometry. λ_{111}, c_{44} are magnetostriction coefficient and shear stiffness constant. In case of TmIG bulk crystal, $K_1 = -0.58\,kJ\,m^{-3}$, $\lambda_{111} = -5.2 \times 10^{-6}$, $c_{44} = 76.6\,GPa$, $M_s = 110\,emu\,cm^{-3}$.

3.2 The growth of $Tm_3Fe_5O_{12}$

PLD is an ideal technique to fabricate TmIG thin films due to the required high background oxygen pressure.[42] Strain modulation is obtained via a set of commercially available substrates with different lattice parameter (Table 3.2.1). Due to the limitation of the uniform deposition area and to guarantee growth condition for each substrate stay constant, all substrates were diced into $2.5 \times 2.5\,mm^2$ and were grown at the same time to prevent drift of the deposition conditions. The only difference would be the strain coming from substrates, The growth conditions are adjusted to achieve perpendicular anisotropy in all substrates for better comparison. The final details are listed below:

- Laser energy $E = 1.2\,J/cm^2$
- Laser repetition rate $6\,Hz$
- Substrate temperature $850\,^oC$
- Cooling rate after growth $5\,^oC/min$
- O_2 background gas pressure $180\,mTorr$

Table 3.2.1: Nominal in-plane strain values for each substrate.

Substrate	Lattice constant (Å)[1]
$Gd_3Ga_5O_{12}$ (GGG)	12.38
$Y_3Sc_2Ga_3O_{12}$ (YSGG)	12.43
$Gd_{2.6}Ca_{0.4}Ga_{4.1}Mg_{0.25}Zr_{0.65}O_{12}$ (SGGG)	12.48
$Nd_3Ga_5O_{12}$ (NGG)	12.51
$Gd_3Sc_2Ga_3O_{12}$ (GSGG)	12.55

[1] Information was obtained from the manufacturer.

3.3 Strain tuning through structural characterization

Symmetric X-ray diffraction is used to initially assess the quality of each film. Oscillation fringes observed around the film peak indicate high crystallinity and smooth surface (Figure 3.3.1(b)). The estimated out-of-plane lattice parameters $a\,(2\theta - \omega)$ are shown in Table 3.3.1 with a slight difference from manufacturer values. Reciprocal space mapping around 624 peaks is performed to confirm the epitaxy relationship between film and substrate. A close inspection on the Q_x value of each film reveals a small shift in the films' values grown on SGGG, NGG and GSGG substrates, indicates a small relaxation in each film. The step size in Q_x is 6.56×10^{-5} Å. The shift in film grown on GSGG ($\Delta Q_x = 1.6 \times 10^{-4}$ Å $\iff \Delta a = 9 \times 10^{-3}$ Å) is considered significant which cause degradation in magnetic performance that can be observed from magnetometry data in the next section. Thickness of each film is estimated using X-ray reflectometry (Figure 3.3.3), which reveals relatively uniform thicknesses across all films (Table 3.3.1) and low surface roughness. This was further confirmed by atomic force microscopy scan, which also reveals extremely smooth surface (root mean square (RMS) $< 150\,pm$) with the exception of the film grown on SGGG that reveals unique topographic features (Figure 3.3.4).

From RSM, both in-plane $a\,(Q_x)$ and out-of-plane $a\,(Q_z)$ can be calculated, with the assumption that the film is strained in-plane with in-plane lattice constant matched with

Table 3.3.1: Thickness of TmIG films estimated from X-ray reflectometry.

Substrate	Thickness (nm)
GGG	17.0
YSGG	16.7
NGG	17.0
SGGG	17.0
GSGG	17.1

that of the substrate. This results in a change in out-of-plane lattice spacing d_{111} (the cube's diagonal) and the distortion of the cubic edges (AB, BC, BD) (Figure 3.3.1(a)). The distortion angle can be calculated geometrically as:

$$cos\beta = \frac{2BC^2 - AC^2}{2BC^2} \tag{3.3.0.1}$$

where $AC = a\sqrt{2}$ and $BC = \left[\left(\frac{d_{111}}{3}\right)^2 + \frac{2a^2}{3}\right]^{1/2}$, a is the cubic lattice parameter of the substrate. The distortion angles β are found to be larger than 90 degrees which indicates that the films experience tensile in-plane strain (and compressive out-of-plane strain).

3.4 Anisotropy tuning

Room temperature magnetometry measurement were run on all samples with applied field parallel (in-plane) and perpendicular (out-of-plane) to the films' surface. Out-of-plane field scans show perpendicular magnetic anisotropy in comparable saturation magnetization across all films except the one grown on GSGG substrate. The saturation magnetization versus distortion angle β is shown in Figure 3.4.1. Below $\beta = 90.74^o$, the saturation magnetization stays approximately constant until suddenly drops at $\beta = 91.17^o$. While unclear, this may be explained by the small relaxation in TmIG film grown on GSGG which is observed in RSM scan discussed above (Figure 3.3.2).

Table 3.3.2: Lattice constants of film and substrate, calculated from different X-ray diffraction techniques, unit in Å, adapted from [21].

Substrate	$a_{substrate}$ $(2\theta-\omega)$ [1]	a_{film} $(2\theta-\omega)$ [2]	$a_{substrate}\,(Q_x)$ [3]	$a_{substrate}\,(Q_z)$ [4]	$a_{film}\,(Q_z)$ [5]	β
GGG	12.38	12.31	12.37	12.39	12.32	90.17
YSGG	12.46	12.24	12.4	12.48	12.25	90.47
SGGG	12.48	12.22	12.47	12.49	12.22	90.74
NGG	12.49	12.20	12.45	12.52	12.22	90.71
GSGG	12.56	12.15	12.54	12.57	12.16	91.17

[1] (out-of-plane lattice parameter of substrate) determined from d_{444} spacing of substrate peak from $2\theta-\omega$ scan.

[2] (out-of-plane lattice parameter of thin film) determined from d_{444} spacing of film peak from $2\theta-\omega$ scan.

[3] (in-plane lattice parameter of substrate) determined from the RSM Q_x value of each substrate.

[4] (out-of-plane lattice parameter of substrate) determined from the RSM Q_z value of each substrate.

[5] (out-of-plane lattice parameter of thin film) determined from the RSM Q_z value of each film.

The dependence of magnetization on in-plane magnetic field is investigated next for anisotropy energy calculation (Equation (3.1.0.5)) with anisotropy field being defined as magnetic field required to saturate the magnet. Figure 3.4.2 shows the magnetization of each film as a function of in-plane applied field. The saturation field is determined from the peaks of second derivative. The change in anisotropy field with distortion angle β is plotted in Figure 3.4.3(a). The anisotropy field tends to increase with increasing distortion angle with the exception of GSGG and SGGG. Due to their direct relationship, anisotropy

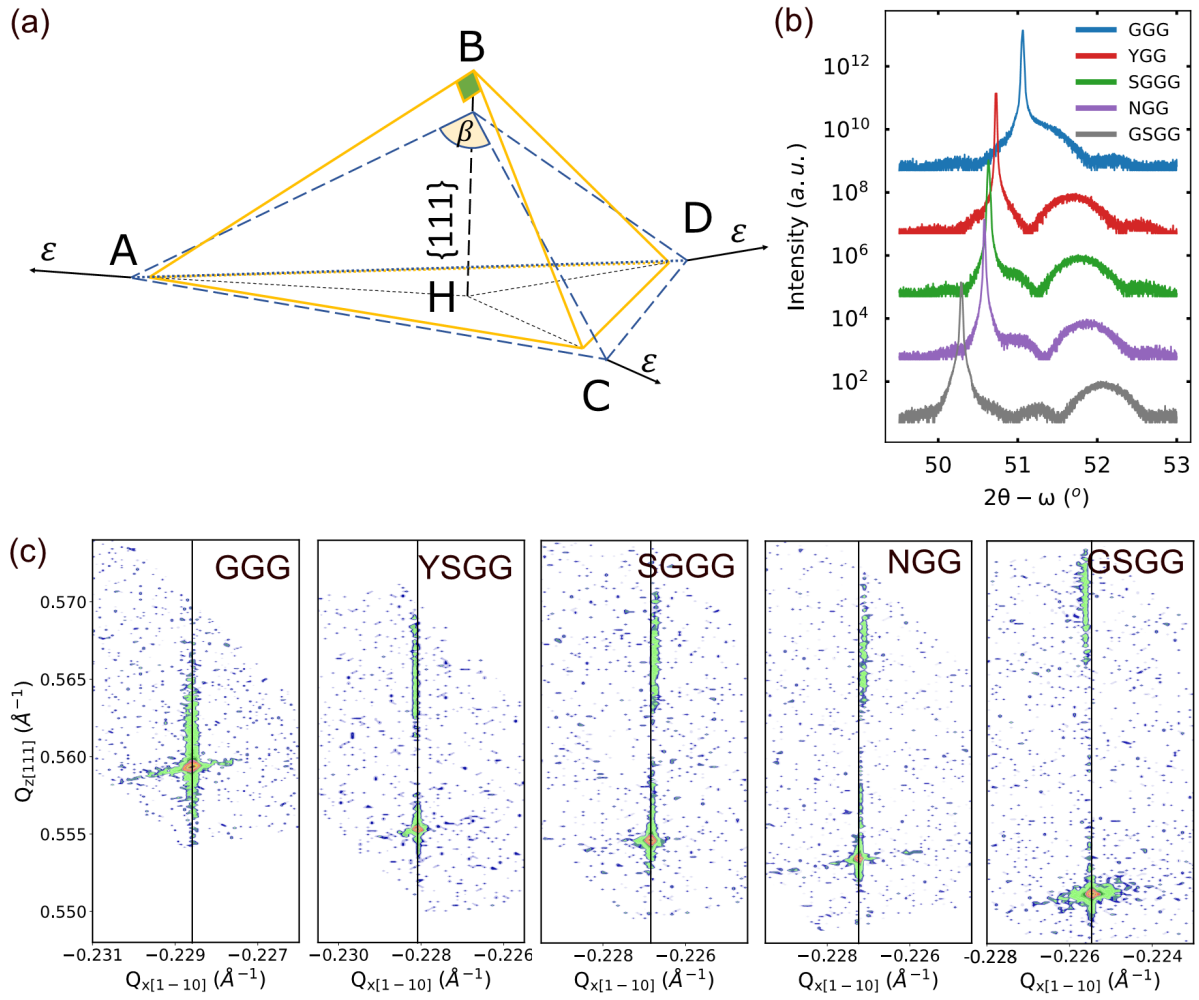

Figure 3.3.1: **(a)** Schematics of strain in TmIG thin film caused by lattice mismatch with the substrate. **(b)** Symmetric X-ray diffraction around 444 peak of 17 nm thick (111) TmIG grown on different substrates. **(c)** Reciprocal space mapping around 444 diffraction peak of both film and substrate. Adapted from [20].

energy also displays the same trend (Figure 3.4.3(a)). With this information, the scaling capability is investigated next. The minimum size a device can reach for each distortion angle is demonstrated in Figure 3.4.3(d). The minimum device size could be achieved within this tuning window is approximately $23 \times 23\,nm^2$, which is still above the desired value ($10 \times 10\,nm^2$). This tuning window is illustrate. with strain independently within our growth conditions, and can be expanded further by fine tuning different growth parameters

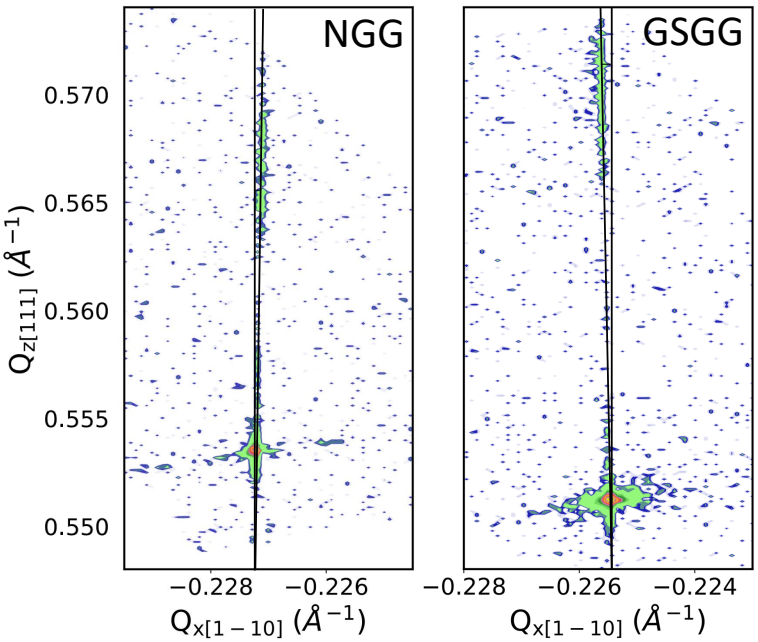

Figure 3.3.2: Zoom-in of RSM scans in NGG and GSGG substrates, showing a slight relaxation in the film lattice, adapted from [21].

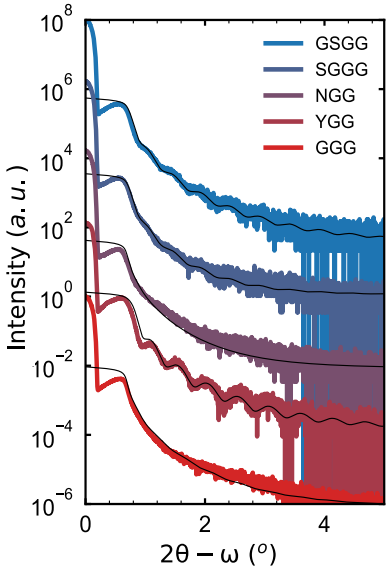

Figure 3.3.3: X-ray reflectivity of TmIG on different substrates, solid back lines are fitting data, adapted from [21].

such as oxygen background pressure.

To further assess the material property, contribution from mangetoelastic energy is as-

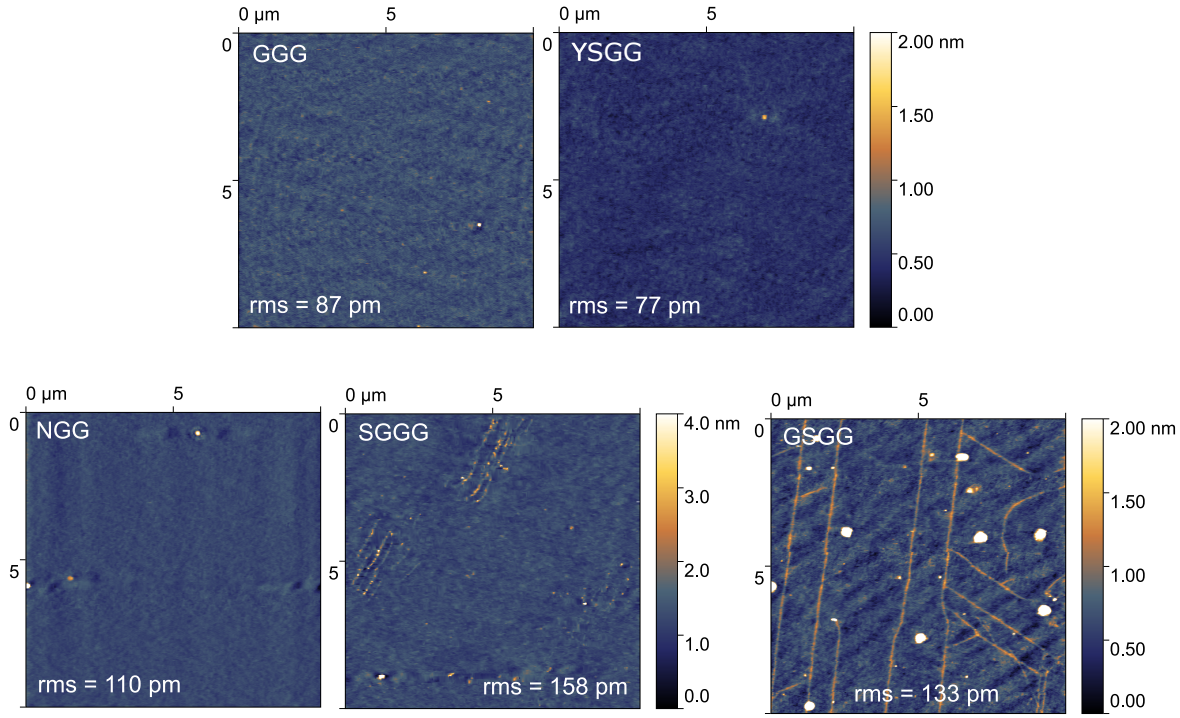

Figure 3.3.4: Topography of the TmIG films grown on different substrates, adapted from [21].

sessed next. Magnetoelastic constant $B_2 = 3\lambda_{111}c_{44}$ reflects the relationship between magnetization and lattice deformation. Figure 3.4.3(c) reports B_2 values for each distortion angle. We see that magnetoelastic constant stays relatively constant until the distortion angle reaches $\sim 90.74^o$. The small B_2 values in GSGG and SGGG justify the small anisotropy fields in spite of the contribution from large lattice distortion.[21] The difference between bulk and thin film values can be explained by several reasons: thin films are clamped to substrate and therefore are not free to deform in-plane but free to deform out-of plane; surface magnetostriction and other surface effects (structural and chemical defects) may become significant at thin film limit. Concern of composition variance effect on anisotropy changes is investigated by X-ray photoelectron spectroscopy (Figure 3.4.4). The data shows that there is no significant difference in composition of films and the target within the error of the analysis, yet the deficiency of Fe is evident and uniform amongst all.

In summary, we have explored the evolution of magnetic anisotropy in rare earth garnet

TmIG, (111)-oriented single crystal thin film, subjected to systematic variation of in-plane strain. In general, the anisotropy energy increases with increasing strain, except in the case of SGGG, where the lattice experiences significant relaxation and a significant drop in its saturation magnetization. We have demonstrated the tuning window for anisotropy energy, and thus the tuning window for the minimum device size that can be reached, within our growth condition and setup. The magnetic anisotropy field is shown to increase up to 14 times while the magnetoelastic constant B_2 can reach value that is 2x larger than bulk value.

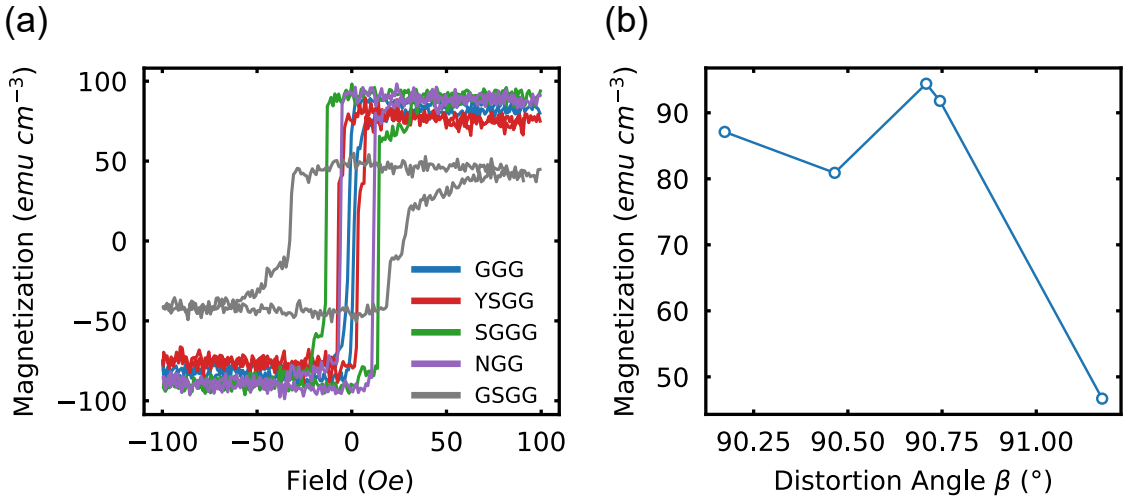

Figure 3.4.1: **(a)** Room temperature out-of-plane magnetization versus magnetic field of 17 nm TmIG thin film on different substrate. **(b)** Saturation magnetization versus distortion angle β. Adapted from [20].

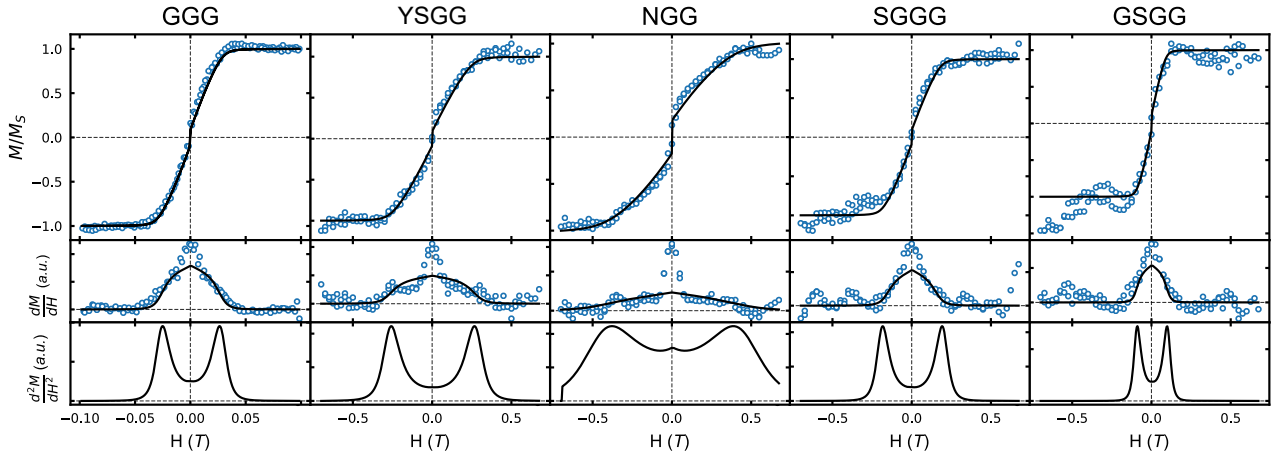

Figure 3.4.2: Top row Room temperature, in-plane magnetization vesrus magnetic field scans of 17 nm TmIG grown on different substrates. The open circle is experimental data and the black line is fitted data following the Stoner-Wohlfarth microspin model. The curvature of the hysteresis loop is from an 5^o offset from the in-plane hard axis due to experimental setup. **Middle row** First derivative of in-plane loops (points), shown with first derivative of the calculated fits (black line). **Bottom row** Second derivative of the fitted data in top row. Anisotropy field is determined from the peaks of second derivative with a field resolution of 1 Oe. Adapted from [21].

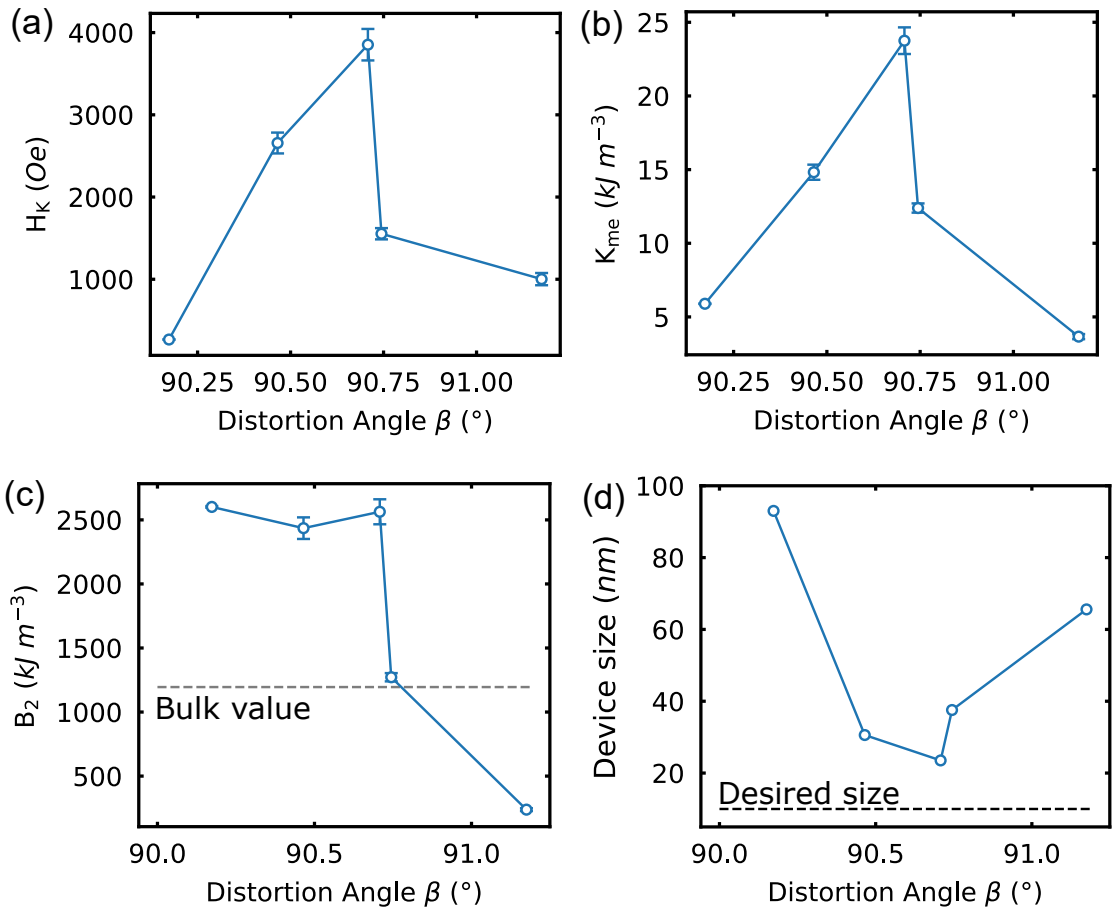

Figure 3.4.3: **(a)** Anisotropy field H_K, **(b)** magnetoelastic energy K_{me}, **(c)** magnetoelastic constant B_2 and **(d)** device size as a function of distortion angle, adapted from [21].

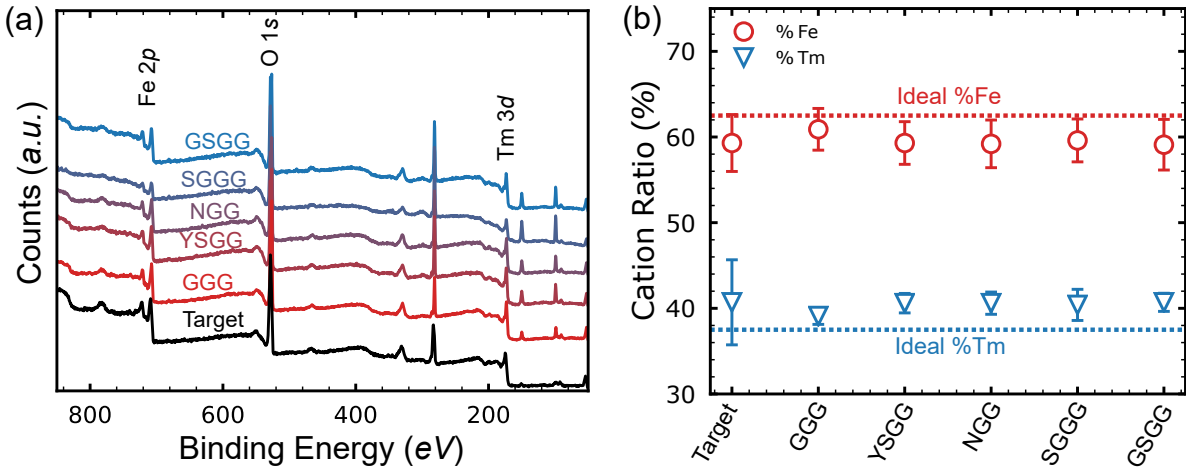

23

Figure 3.4.4: X-ray photonelectron spectroscopy data of TmIG target and thin films on different substrates. **(a)** Raw data and **(b)** estimated ratio of Fe and Tm element in each sample, adapted from [21].

Chapter 4

Magneto-electrics Cr_2O_3

4.1 Background

4.1.1 Crystal structure and magnetic structure

Cr_2O_3 belongs to the space group $R\bar{3}c$, possessing 3-fold symmetry and an inversion center, and has lattice parameters: $a = 4.9530$ Å, $c = 13.5884$ Å. In the primitive cell, there are 4 Cr^{3+} atoms aligning along the body diagonal. Here c axis is of interest because of its coincidence with its magnetic structure (Figure 4.1.1(a)).

Cr_2O_3 crystal also has corundum structure, in which each chromium atom is surrounded by a distorted oxygen octahedron (Figure 4.1.1(b)). This structure combined with the fact that Cr^{3+} standing alone is a magnetic atom contributes to the formation of magnetic group $\bar{3}'m'$. The magnetic structure of Cr_2O_3 is antiferromagnetic as shown in Figure 4.1.1(b), with Néel temperature of bulk single crystal at $307\,K$.[22] Cr_2O_3 is the very first material which was proved to possess magnetoelectric effect both theoretically and experimentally.[55, 56] The breaking of time reversal and space inversion symmetry in Cr_2O_3 permits the magneto-electric energy term. In addition to that, the antiferromagnetic structure makes it become a potential candidate for electric field switching using exchange bias, which will be discussed in a later section.

Assuming a perfect structure with c-plane being parallel to the film surface, there will be an uncompensated magnetization at the surface (Figure 4.1.1(c)). The crystal structure of (Figure 4.1.1(a)) can be considered as a structure with alternate layers of Cr^{3+} atom with opposite spin direction stacking on top of each other. However, this antiferromagnetic structure allows the formation of two opposite antiferromagnetic domains, which cancel out each other and lead to zero net surface magnetization. Magnetoelectric annealing (annealing the sample through Néel temperature under applied magnetic and electric field) is capable of lifting this degeneracy and producing a single domain state at the surface.[22]

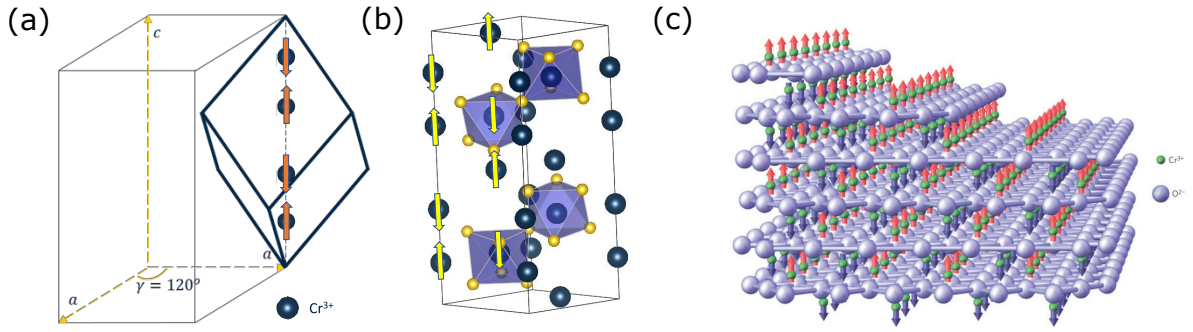

Figure 4.1.1: **(a)** Crystal structure belong to rhombohedral family with 4 Cr^{3+} atoms aligning along c axis. **(b)** Magnetic structure of Cr_2O_3: each Cr^{3+} atom is surrounded by an oxygen octahedron and has spin pointing parallel to each other and perpendicular to the c axis. (Crystal structure was constructed using Vesta software) **(c)** Configuration of surface magnetization of Cr_2O_3, printed with permissions from [22].

4.1.2 Magneto-electricity in Cr_2O_3

Since the first observation of the change in magnetization of a dielectric moving in an electric field by Rontgen [57], both experimental and theoretical studies have directed the focus on the magnetoelectric (ME) effect. The expectation that electric field can be used to directly control magnetization of materials to produce non-volatile, small scale and low-power spintronic devices has greatly increased the amount of work done in this field over recent years.[58, 59] Magnetoelectric materials or heterostructures are essentially systems

exhibiting magnetoelectric response such that a magnetic field (electric field) can be applied to control their polarization (magnetization) directly.

Theory of Magnetoelectric Effect

Following Rivera [60], to describe the density of stored energy or free enthalpy of a crystal, a function $g(H, E, T)$ is used, where H, E,and T are the applied magnetic field, applied electric field and temperature, respectively. Using Taylor expansion or limited Maclaurin series at a constant temperature, $g(H, E, T)$ becomes a function of H, E as described below:

$$-g(H,E,T) = ...P_i^S E_i + M_i^S H_i + \frac{1}{2}\epsilon_o \epsilon_{ik} E_i E_k + \frac{1}{2}\mu_o \mu_{ik} H_i H_k + \alpha_{ik} E_i H_k \qquad (4.1.2.1)$$

where:

$$\epsilon_o, \mu_o : \text{ free space permitivity and permeability}$$

$$P^S, M^S : \text{ spontaneous polarization and magnetization}$$

$$\epsilon_{ik}, \mu_{ik} : \text{ relative permitivity and permeability}$$

$$\alpha : \text{ tensor of linear ME [s/m]; } \alpha_{ik} : \text{ asymmetric in ik}$$

$$\beta : \text{ tensor of bilinear ME [s/A]; } \beta_{ijk} : \text{ asymmetric in jk}$$

$$\gamma : \text{ tensor of bilinear ME [s/V]; } \gamma_{ijk} : \text{ asymmetric in jk}$$

$$\alpha, \beta, \gamma : \text{ are function of temperature only}$$

By differentiating g we achieve total polarization and magnetization of the crystal:

$$P_i = P_i^S + \alpha_{ij} H_j + \beta_{ijk} H_j H_k \qquad (4.1.2.2)$$

$$M_i = M_i^S + \alpha_{ij} E_j + \gamma_{ijk} E_j E_k \qquad (4.1.2.3)$$

From polarization and magnetization equations, it is obvious that when an electric (magnetic) field is applied, there will be changes in magnetization (polarization) of materials. The last two terms of above equations describe the linear and bilinear magnetoelectric effects. However, an energy term is permitted only if it remains invariant under any point symmetry

Table 4.1.1: A list of some materials which possess magnetoelectric effect.

Material	ME coefficient (Gaussian unit)	Temperature (Kelvin)	Reference
$LiCoPO_4$	$\alpha = 6 \times 10^{-4}$	23	H. Schmid (1973, 2000)
Cr_2O_3	$\alpha = 1 \times 10^{-4}$	312	
$Gd_2Fe_5O_{12}$	$\alpha = 4 \times 10^{-6}$	563	
$Y_3Fe_5O_{12}$	$\alpha = 5 \times 10^{-6}$	563	H. Schmid (1973, 2000)
	$\alpha = 9 \times 10^{-3}$	77	M. Fiebig (2005)
$BiFeO_3$	$\alpha = 30$ [a]	643	J. Heron *et al.* (2014)

[a] Value calculated for a heterostructure.

possessed by the crystal or time reversal operation, thus the magnetoelectric effect can only be observed in a limited set of materials. The classification of crystal and magnetic structures has been used to predict and synthesize new materials with the magnetoelectric effect. Ultimately, the magnetoelectric effect occurs in materials that display a Dzyaloshinskii-Moriya interaction which is a manifestation of spin-orbit coupling in low symmetry materials. Table 4.1.1 contains a partial list of materials known to possess magnetoelectric effect. They were discovered both experimentally and theoretically.

Materials possessing a linear magnetoelectric effect is of greater interest than a non-linear magnetoelectric effect because the magnitude of the linear effect is significantly larger than higher-order effects. However, the number of these materials with a critical temperature above room temperature is extremely limited. The most promising room temperature and single-phase materials for electric field control of magnetization are antiferromagnetic and ferroelectric $BiFeO_3$ with giant pseudo-linear magnetoelectric coefficient [45], or currently discovered ferromagnetic and potential pyroelectric $\epsilon - Fe_2O_3$ with giant coercive field [61], or antiferromagnetic $\alpha - Cr_2O_3$ with perpendicular magnetization [55] .

However, the magnitude of magnetoelectric effect is far too low for voltage control as

a stand-alone material and, as most magnetoelectrics are antiferromagnetic insulators, it is difficult to investigate them. An alternative approach is to use hybrid magnetoelectric systems (heterostructures) which permits the amplification of a magnetoelectric effect by coupling the spins of a strong ferromagnetic conductor to the antiferromagnetic order of the magnetoelectric. This coupling is known as interface exchange coupling or, more commonly, exchange bias (which will be discussed further in the next section). An illustration of the magnetoelectric switching of an exchange coupled ferromagnet is given in figure 4.1.2. Since the first electric switching of exchange bias demonstrated in 2005 by Borisov et al. [62] and the wealth of exchange bias studies for the use in hard disk drive, exchange coupled magnetoelectric heterostructures are being investigated. The working temperature of exchange bias (blocking temperature, which will be discussed below) is much lower than the Néel temperature of the antiferromagnet when approaching the ultra thin limit. This makes exchange bias an unattractive switching mechanism for room temperature application. The solution for this problem was proposed by Kosub *et. al.* [14]. Due to the existence of uncompensated surface magnetization, an exchange coupling called proximity effect between Cr_2O_3 and a high spin orbit coupling material (e.g. Platinum) exists. This effect will magnetize the Pt layer which is detectable through anomalous Hall effect (discussed below). This phenomenon does not depend on the thickness of Cr_2O_3 and therefore reflects the Néel temperature of the antiferromagnet.

4.1.3 Exchange bias in heterostructures

The exchange bias effect, first proposed by Meiklejohn and Bean about 60 years ago, describes a magnetic coupling phenomenon that happens at the interface shared by two magnetically order systems, e.g. antiferromagnet and ferromagnet.[62, 63] The main characteristic of an exchange bias representing in a system are:[62]

- A shift of hysteresis loop along its normal position with respect to the applied magnetic field.

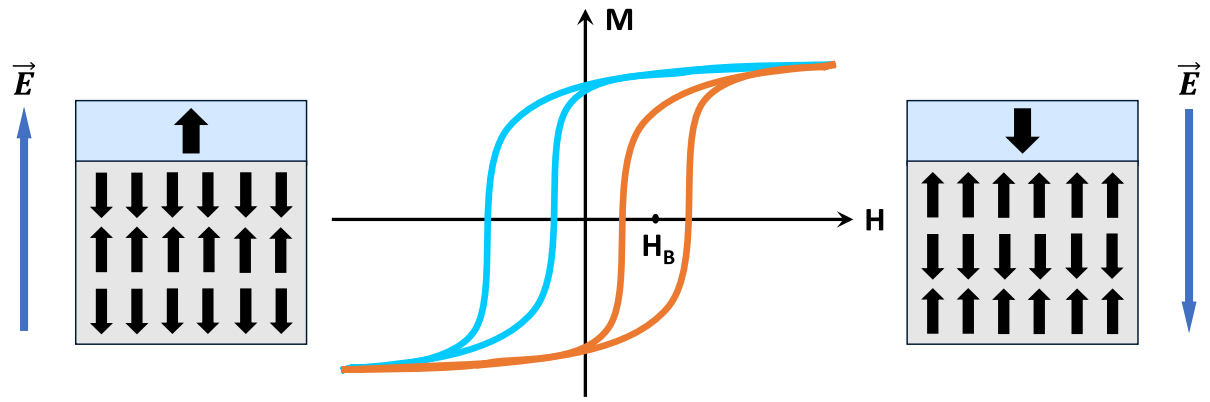

Figure 4.1.2: Schematic of magnetization switching using electric field using magnetoelectric materials. Since the material possess magnetoelectric effect, applying an electric field can switch its magnetization. The ferromagnetic layer on top is also switched in this process through exchange coupling and is used to probe the change in magnetization of magnetoelectric layer.

- The broadening of the hysteresis loop (i.e. an enhancement of coercive field H_c).

The exchange bias field will be generated if the system is grown or cooled through the Néel temperature in the presence of an external magnetic field.

The shift of hysteresis loop or the presence of an exchange bias field helps keep the magnetization of the ferromagnetic layer stable. From the ideal model of Meiklejohn – Bean of exchange bias, exchange bias field can be expressed as: [62]

$$H_{EB} = -\frac{J_{EB}}{\mu_o M_F t_F} \tag{4.1.3.1}$$

where $J_{EB}\,[J/cm^2]$ is the interface exchange energy per unit area, M_F and t_F are the saturation and thickness of the ferromagnetic layer, respectively. By changing the thickness of the ferromagnetic layer, one can expect to tune the exchange bias field accordingly.

The broadening of the hysteresis loop is another consequence of exchange bias between antiferromagnetic and ferromagnetic layer. No theory has been able to explain adequately

experiment results for different exchange bias system.[64] However, one can generally presume that the coercive field should depend on the thickness of the ferromagnetic layer and the exchange energy between two layers. Depending on the specific system, as well as different theoretical assumptions, the thickness of the antiferromagnetic layer also affects the enhancement of the coercive field, however there is no general rule for the trend of this parameter.[64, 62, 65] For electric field switching of exchange bias, the crystallinity of $\alpha - Cr_2O_3$ is very important because a single crystal $\alpha - Cr_2O_3$ will have higher breakdown voltage and therefore increases the electric field threshold for the switching process.

According to Meiklejohn-Bean and spin glass model, the exchange bias and coercive fields are the result of a rather complicated combination of the antiferromagnetic anisotropy energy (K_{AF}), the thickness of the antiferromagnetic layer (t_{AF}), interface exchange energy (J_{eb}), and a conversion factor, f, related to interface disorder/frustration (f is a factor between 0 and 1 and represents the degree of interface spin disorder and often assumed to be 1).[62]

$$R = \frac{K_{AF} t_{AF}}{f J_{eb}} \tag{4.1.3.2}$$

When $R \geq 1$, exchange bias is expected, while when $R < 1$ exchange bias is predicted to be suppressed and coercivity enhanced. As R defines the strength of the antiferromagnetic layer, the competition between the change in spin structure (affects K_{AF}, J_{eb}) and the surface reconstruction (affects J_{eb}, f) impacts directly the behavior of exchange field at low temperature.

The blocking temperature, as mentioned above, is defined as the temperature where above that, exchange bias phenomena disappears.[62] This temperature is general lower than the Néel temperature of the antiferromagnet layer, especially at a very low thickness. The condition for exchange bias to exist can be derived from Equation (4.1.3.2) in which the anisotropy energy K_{AF} of the antiferromagnet layer needs to exceed a certain threshold value ($K_{AF,critical} = f J_{eb}/t_{AF}$). This condition reflects the dependence between layer thickness and the blocking temperature, also known as finite size effect.[62]

4.1.4 Magnetic proximity effect

Magnetic proximity effect is also an interface phenomena in which a penetration of spin polarization, from a ferromagnetic layer into a nonmagnetic, high exchange-enhance spin susceptibility (high spin orbit coupling), occurs. The prominent materials that possess high spin orbit coupling are heavy metal such as Ta, Pt, Pd and recently attracting attention, transition metal dichalcogenides. Due to the existence of non-compensated surface spin, Cr_2O_3 surface acts as a ferromagnet which can generate ferromagnetism in a proximate nonmagnetic layer. This reduce the complexity of the heterostructure and also enhance the resilience of the structure against external magnetic field, since the field required to demagnetize the magnet will be the field required to demagnetize the antiferromagnetic layer, which is usually large.[48]

Anomalous Hall effect

The aforementioned induced magnetization in heavy metal that comes in contact with Cr_2O_3 surface can be detected based on the phenomenon called anomalous Hall effect (AHE). In contrary to ordinary Hall effect, which requires external magnetic field, AHE can be detected in conducting material with net magnetization. With the same measurement configuration with Hall effect, an applied current would generate a transverse Hall voltage in conducting magnetic materials. When the magnetization direction changes under an applied field (magnetic or electric), the resistance changes accordingly (magnetoresistance). The detected Hall voltage reflects the direction of magnetization and the magnitude of magnetic moment. Since the magnetization in Pt layer is decided by the antiferromagnetic order, below Néel temperature, a very large magnetic field is needed to rotate the magnetic moment. Above the Néel temperature, the invariant Hall resistance is zero at zero applied magnetic field because there is no spontaneous net magnetization in Pt layer (Figure 4.1.3(b)). This is a highly effective way to probe the magnetization switching and Néel temperature in the insulating Cr_2O_3 (Figure 4.2.1(c).[23]

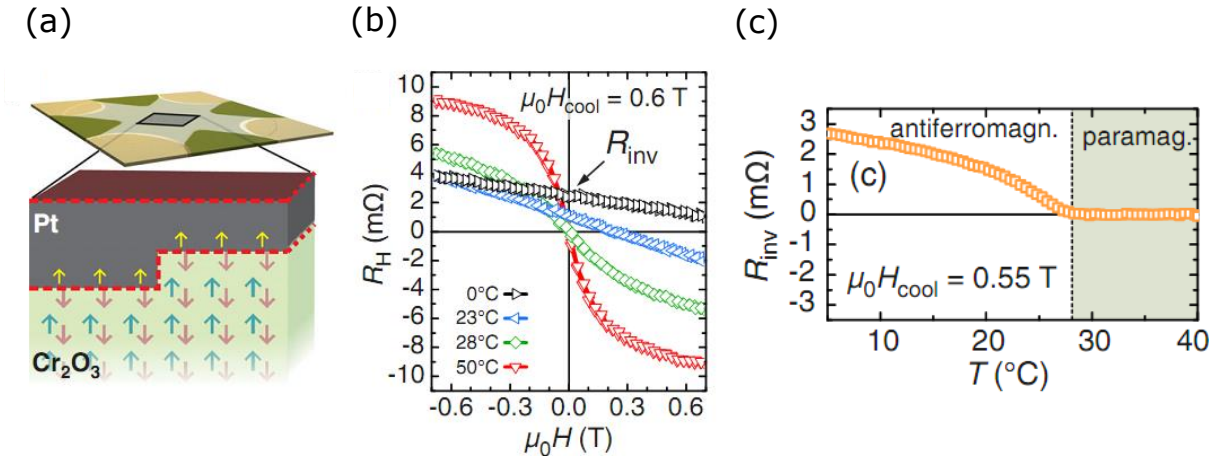

Figure 4.1.3: **(a)** Proximity effect in Pt/Cr_2O_3 heterostructure and anomalous Hall setup using spinning current offset method. **(b)** Invariant Hall resistance reflect the net magnetic moment at zero applied field. At temperature above Néel temperature, only a small magnetic field needed to saturate the moment in Pt layer. **(c)** Néel temperature detection in Cr_2O_3 using the anomalous Hall voltage. The thickness of Cr_2O_3 film in this work is 250 nm. Printed with permission from [23].

4.2 Single-crystal growth of Cr_2O_3 on an electrode

The growth of single crystal film Cr_2O_3 on Al_2O_3 substrate is well studied and discussed elsewhere.[66, 48] In our deposition system, the perfect condition is found to be at 135 mJ laser energy, 6 Hz repetition rate, 30 $mTorr$ oxygen background gas pressure and 700 ^oC substrate temperature. The films grown at this condition possesses highly crystalline, single crystal structure and a smooth surface (as shown in X-ray diffraction data, Figure 4.2.1).

Initially, electrode for electric field control of magnetization in Cr_2O_3 is chosen to be Pt for its good conductivity and the pseudo hexagonal structure in (111) growth direction, which matches Cr_2O_3 crystal structure. The first choice substrate for Pt was $SrTiO_3$ (111) (STO) due to the similar cubic lattice and a excellent lattice match ($\approx$ 0.4%). Within condition range, although Pt is highly crystalline (Figure 4.2.2(a)), it is crystallographically twinned (1%) and Cr_2O_3 is 100% twinned when grown on top (Figure 4.2.3(a)). The next

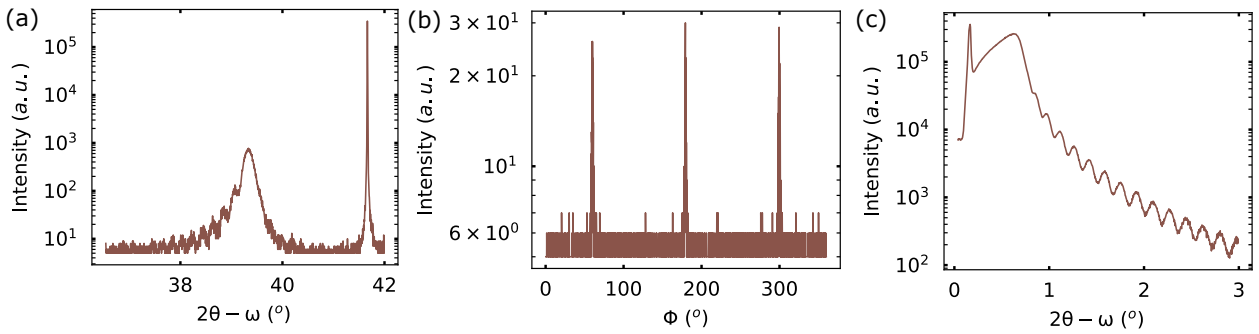

Figure 4.2.1: **(a)** X-ray diffraction of thin film Cr_2O_3 grown on (0001) Al_2O_3, oscillation fringes around the film peaks indicates good crystallinity, **(b)** Phi scan around 014 peak of Cr_2O_3 shows 3-fold symmetry which is signature of single domain crystal, **(c)** X-ray reflectivity of the film.

approach is finding condition to achieve single crystal Pt electrode. Following previous work by Trassin *et al.* [6], Pt was grown on YSZ (111) (Y_2O_3 stabilized ZrO_2, 8% mole Y_2O_3) with a Ti buffer layer for adhesion purpose. The first few attempt of Pt grown on YSZ were unsuccessful. Pt was twin and Cr_2O_3 is also twin. However, Φ scan of the structure shows a 30^o rotation of Cr_2O_3 lattice, resulting in a reduction in strain from 10.7% to 3.1% (Figure 4.2.3(b) and Figure 4.2.4). It was found that thickness of Ti is important to the formation of twin domains in Pt. By optimizing Ti thickness to be within 4 to $6\,nm$, smooth single crystal Pt was achieved (Figure 4.2.2(b) and Figure 4.2.3(c)). With single crystal Pt and reduced strain, however, Cr_2O_3 grown on the improved Pt layer shows no sign of reducing twin (Figure 4.2.3(c)).

The search for a more suitable electrode replacing Pt began. Kosub *et al.* (2017) shows that using V_2O_3, a conducting oxide, as an electrode, the twinning in Cr_2O_3 is reduced. V_2O_3 has the same hexagonal structure and a good lattice match with Cr_2O_3 (strain $\approx 0.15\%$). As a Metal-Insulator-Transition oxide, the growth of V_2O_3 has been intensively studied in literature.[67, 68, 69] In our PLD sytem, V_2O_3 is deposited from a V_2O_5 target in Ar background gas pressure. The fine tuned condition for V_2O_3 is $195\,mJ$ laser energy, $8\,Hz$ repetition rate, $10\,mTorr$ argon background gas pressure and $400\,^oC$ substrate temperature. The

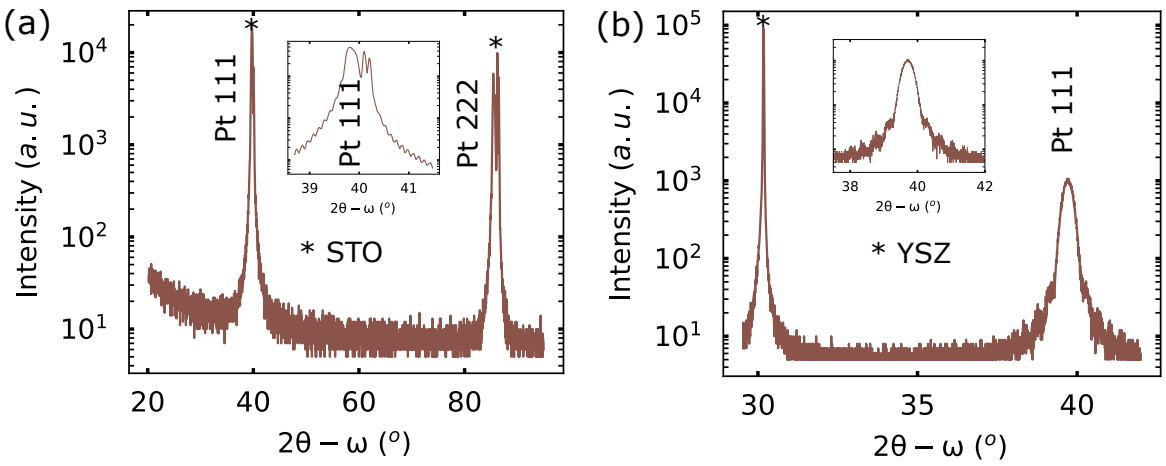

Figure 4.2.2: X-ray diffraction of **(a)** Pt grown on STO (111) and **(b)** Pt grown on YSZ (111) with Ti buffer layer. Insets are zoom-in plots around the Pt (111) peak, revealing oscillation fringes which indicate smooth surface and high crystallinity.

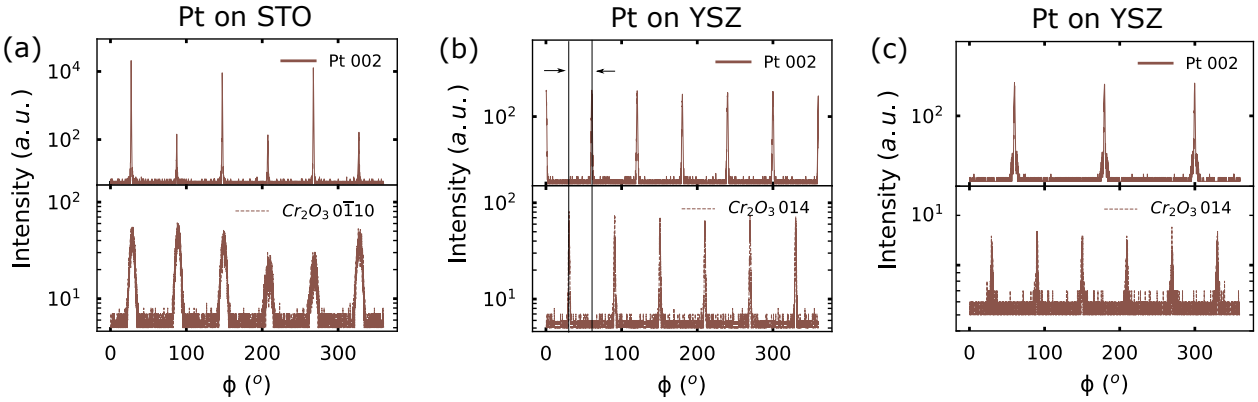

Figure 4.2.3: Φ scan of Pt and Cr_2O_3 **(a)** 1% twin Pt grown on STO (111) substrate, **(b)** twin Pt grown on YSZ (111) with Ti buffer layer, showing a 30^o rotation in Cr_2O_3 lattice, **(c)** single crystal Pt grown on YSZ (111) with Ti buffer layer.

challenge lies in finding the compatible growth condition for Cr_2O_3 without compromising the V_2O_3 underneath. The growth condition for Cr_2O_3 on V_2O_3 is kept the same with Cr_2O_3 grown on Al_2O_3 except the substrate temperature, which was reduced to $650\,^oC$ to avoid degradation in V_2O_3. Howver, V_2O_3 reacts easily with oxygen to form V_2O_5 which melts at temperature even lower than its melting point ($690\,^oC$) (Figure 4.2.5(b)). Reduction of

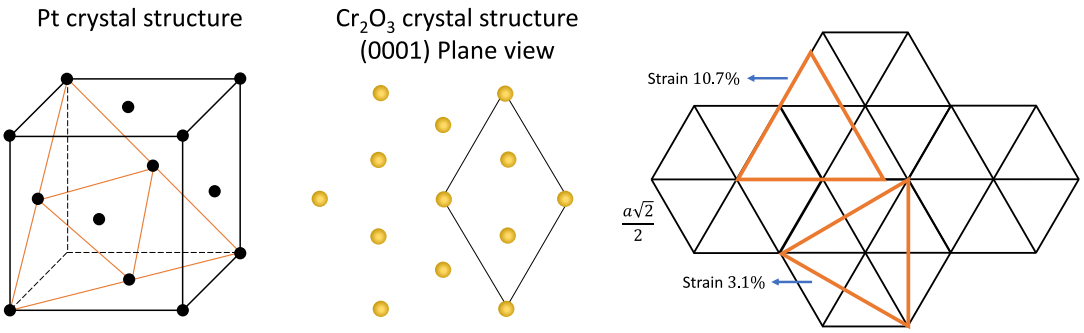

Figure 4.2.4: Crystal structure of Pt (**left**), Cr_2O_3 (**middle**) and calculated strains for different orientations of Pt with respect to Cr_2O_3 lattice (**right**).

growth temperature to 500 ^oC favors the formation of VO_2 (Figure 4.2.5(a)). By switching to argon gas, V_2O_3 was fully protected with epitaxial grown Cr_2O_3. The final growth condition of Cr_2O_3 on V_2O_3 was tuned using surface roughness from AFM and XRD measurements (peak position and oscillation fringes, Figure 4.2.6(a)). Quality of V_2O_3 is considered comparable with previous report from literature through comparison of the full width half max of V_2O_3 peak (Figure 4.2.6(b)).[69] Cr_2O_3 thin film exibits high quality crystal with oscillation fringes around the film peak and 3-fold rotation which indicates single crystal growth. The surface/interface in the heterostructure is smooth according to both oscillation fringes and surface topography (Figure 4.2.7).

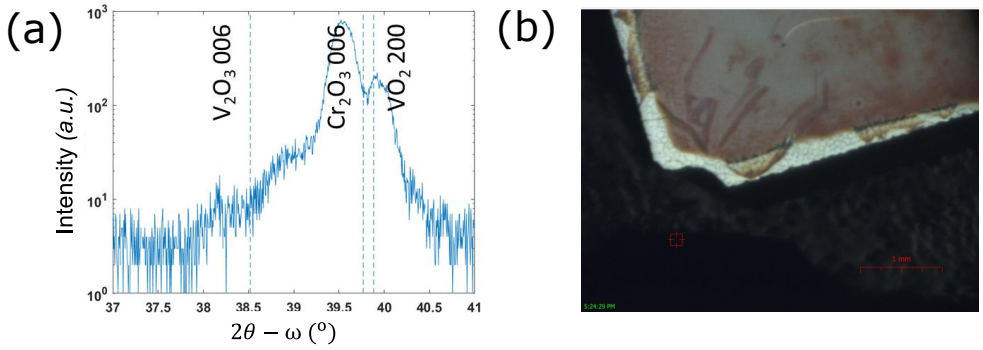

Figure 4.2.5: **(a)** X-ray diffraction of Cr_2O_3 grown on V_2O_3, Cr_2O_3 was grown in oxygen, the peak indicates the formation of VO_2 phase. **(b)** V_2O_3 oxidized into V_2O_5 and melted at the edge.

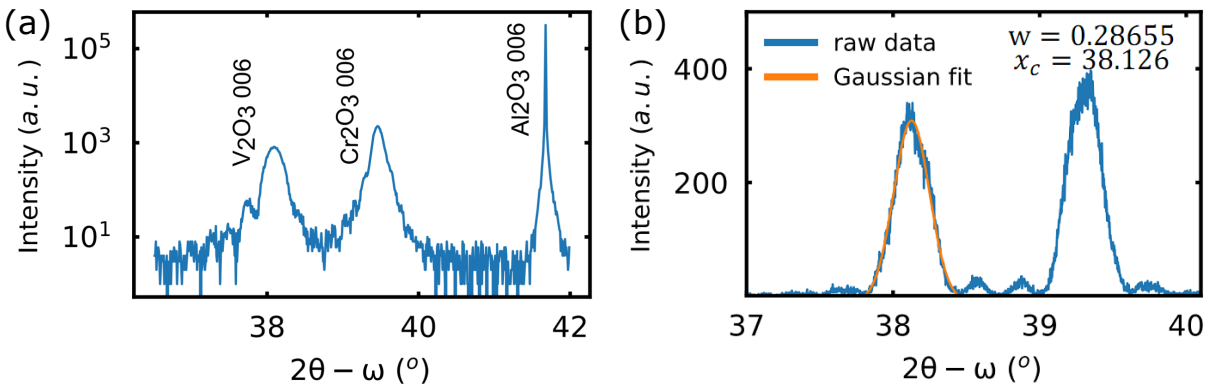

Figure 4.2.6: **(a)** Zoom-in X-ray diffraction scan of Cr_2O_3 grown on V_2O_3 on Al_2O_3 (0001) substrate. **(b)** Fitting of the V_2O_3 peak with the full width half max value w and peak position x_c.

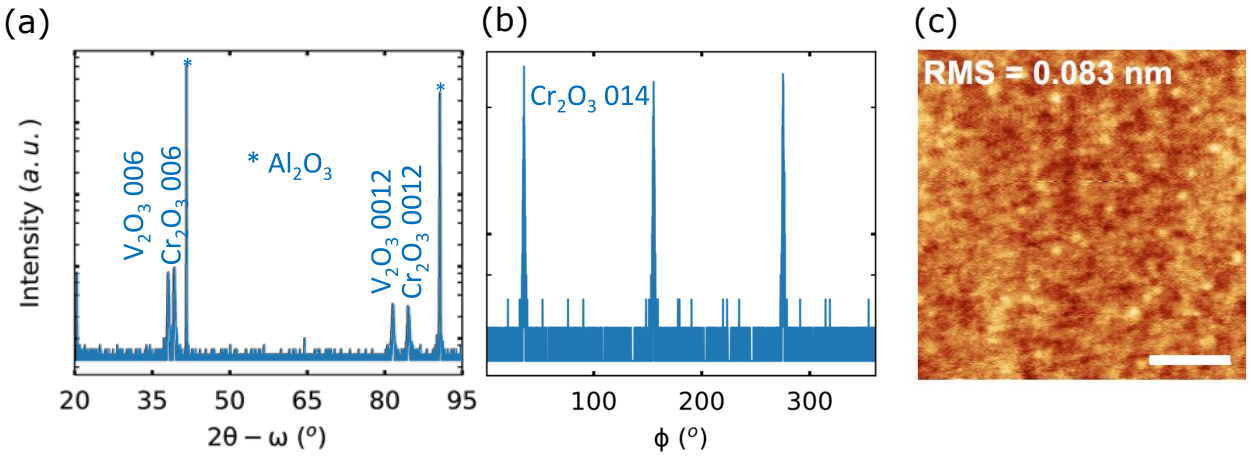

Figure 4.2.7: **(a)** Full range X-ray diffraction of Cr_2O_3 grown on V_2O_3 on Al_2O_3 (0001) substrate. **(b)** ϕ scan around Cr_2O_3 014 showing a 3-fold symmetry. **(c)** Topography of Cr_2O_3 grown on V_2O_3 with surface roughness 0.083 nm. Adapted from [21].

4.3 Electrical properties of sub 100-nm-thin Cr_2O_3 film

Electrical properties of Cr_2O_3 grown on V_2O_3 are investigated next to assess its potential for electric field control of magnetization. Circular electrodes are deposited in the same PLD

system. Ti ($6\,nm$)/Pt ($120\,nm$) circular pads are defined using standard photolithography and lift-off process. Leakage current is tested using a Radiant Technologies Precision Multiferroic II with minimum current detection of 1 pA for a 2 second integration period. Figure 4.3.1(a) plot the mean resistivity of Cr_2O_3 thin films on different electrodes and different thicknesses. $30\,nm$ thick single crystal Cr_2O_3 shows noticeable improvement in leakage current compared to $70\,nm$ thick twin Cr_2O_3. At $60\,nm$, Resisitivity of single crystal Cr_2O_3 film reach the the bulk value ($10^{12}\,\Omega$), demonstrating significant enhancement in dielectric performance with the absence of twin domains. When varying the electrode sizes, leakage current increases with increasing the size, which can be justified by the increase in the possibility of encountering a defect.

Breakdown tests were performed using the same probe station setup but with Keithley sourcemeter. The test were done on electrode pads that show high resistivity performance. Break down electric field in single crystal thin films at both thicknesses. Especially, for $60\,nm$ film, the breakdown field ranges from 170 to $225\,MV\,m^{-1}$, which is comparable to the reported value of a $500\,nm$ thick twinned Cr_2O_3 at $200 \times 200\,\mu m^2$ electrode.[4] This value is $\sim$ 20% of the reported bulk value ($1000\,MV\,m^{-1}$) (Figure 4.3.1(a)).[70]

4.4 Magnetic properties of sub 100-nm-thin Cr_2O_3 film

Intrinsic magnetic properties in Cr_2O_3 at room temperature is probed directly using second harmornic measurement (Figure 4.4.1(a)). The sample of interest is a 30-nm-thick single crystal Cr_2O_3 on V_2O_3. The magnetic point group $\bar{3}'m'$ of Cr_2O_3 below the Néel temperature permits both magnetic (χ_m) and electric (χ_e) dipole susceptibility tensors. The expressions of each contribution are:

$$I_{MD} \propto |-\chi_m E_i^2(cos2\phi_i sin\phi_s + sin2\phi_i cos\phi_s)|^2 \tag{4.4.0.1}$$

$$I_{ED} \propto |-\chi_e E_i^2(sin2\phi_i sin\phi_s - cos2\phi_i cos\phi_s)|^2 \tag{4.4.0.2}$$

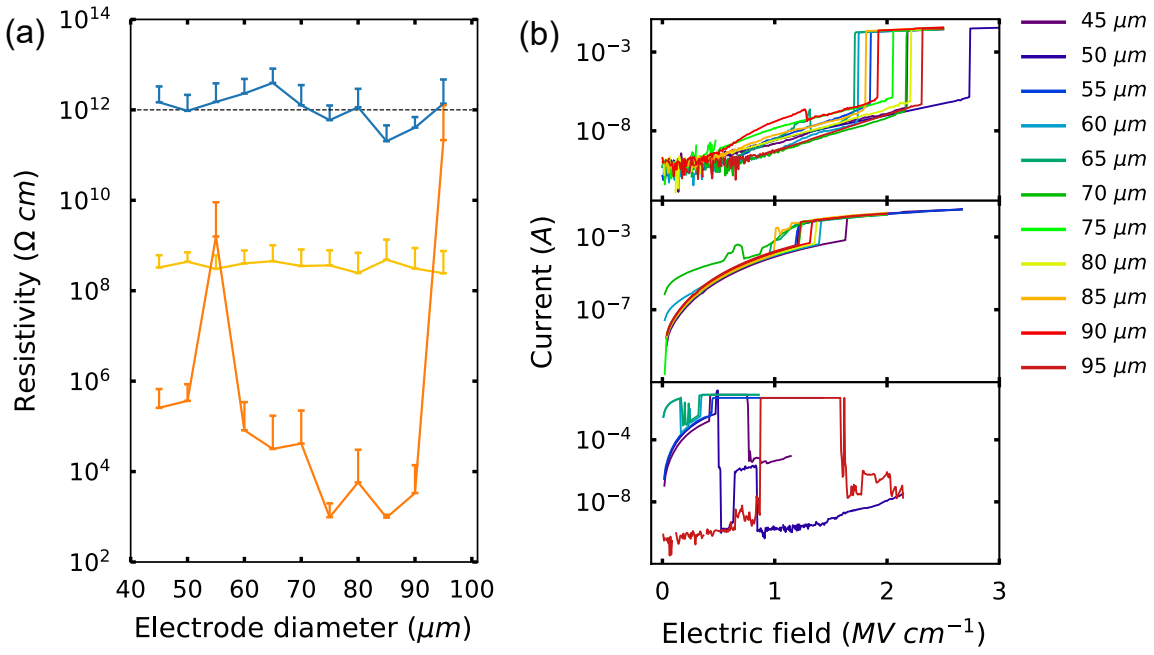

Figure 4.3.1: **(a)** Mean resistivity of 60 nm thick Cr_2O_3 (blue), 30 nm thick Cr_2O_3 (yellow) on (0001)-oriented V_2O_3/Al_2O_3 and 70 nm thick Cr_2O_3 on (111)-oriented Pt/Ti/YSZ (orange). The black dash line is the bulk value. **(b)** Breakdown electric field of low leakage devices in 60 nm thick Cr_2O_3 (top panel), 30 nm thick Cr_2O_3 on V_2O_3/Al_2O_3 (middle panel), and 70 nm thick Cr_2O_3 on Pt/Ti/YSZ (bottom panel) at different electrode diameters. Adapted from [21].

where E_i, ϕ_i, and ϕ_s are the electric field of the incident beam, the incident angle between the crystal axis $[11\bar{2}0]$ and the incident electric polarization, and the angle between the crystal axis $[\bar{1}100]$ and the generated second harmonic electric polarization. The magnetic dipole signal is the signature of centrosymmetric point group $\bar{3}m$ in Cr_2O_3 and therefore exists above Néel temperature. The electric dipole signal, on the other hand, reflects the noncentrosymmetric magnetic order in Cr_2O_3 which is allowed only below Néel temperature. [71, 72] By fixing the analyzer along x ($[11\bar{2}0]$) or y ($[\bar{1}100]$) direction, the $cos\phi_s$ (or $sin\phi_s$) goes to 0, magnetic and electric dipole signal then become dependent of the incident angle ϕ_i only, following $sin2\phi$ (or $cos2\phi$) and $cos2\phi$ (or $sin2\phi$), respectively. By comparing the

simulated result with the experimental rotational-anisotropy data (figure 4.4.1(a)), the existence of electric dipole is confirmed, which follows the $cos2\phi$ ($sin2\phi$) dependence of incident angle ϕ_i. This is a direct evidence that the film exhibits symmetry which is consistent with magnetic order of bulk Cr_2O_3 at the measured condition.

As interface exchange is an important part of integrating Cr_2O_3 with different magnetic systems, heterostructure of Cr_2O_3 with ferromagnetic permalloy (Py) is investigated next. The system went through an in-plane magnetic field cooling of $\pm 5000\,Oe$ from $350\,K$ to $10\,K$. The enhancement of the permalloy's coercive field is clearly demonstrated in Figure 4.4.1(b). The evolution of the coercive field and exchange bias as a function of temperature is shown in Figure 4.4.1(c). The antiferromagnet anisotropy axis in our thin film Cr_2O_3 aligns along c-axis. The training field in this case, however, is aligned perpendicular to the c-axis which is expected to induce a small canting of the Cr moments. This enables the observed exchange bias field with the in-plane ferromagnet permalloy. The exchange bias field disappeared at temperature above $285\,K$, which is lower than the Néel temperature in bulk crystal ($307\,K$). This result is in agreement with the above discussion of finite size effect on blocking temperature in exchange bias systems. At temperature below 150_K, there is an abnormal behavior when the exchange bias field reduces gradually when the temperature decreases, meanwhile the coercive field continues to increases. Previous studies have shown possible explanation for this phenomenon which related to the change in magnetic structure at low temperature [56] or a structural rearrangement at the (0001) surface of Cr_2O_3 [73, 74]. Detailed work focusing on analyzing individual factors in (4.1.3.2) is necessary to understand this situation.

4.5 Néel temperature investigation

Magnetic field dependence of anomalous Hall signal in Pt is first investigated to paint a full picture of different error types in the measurement setup. A thin Pt layer ($\sim$ 2 to $2.5\,nm$) is deposited in situ on top of Cr_2O_3 ($60\,nm$)/V_2O_3 heterostrucutre at room temperature. This

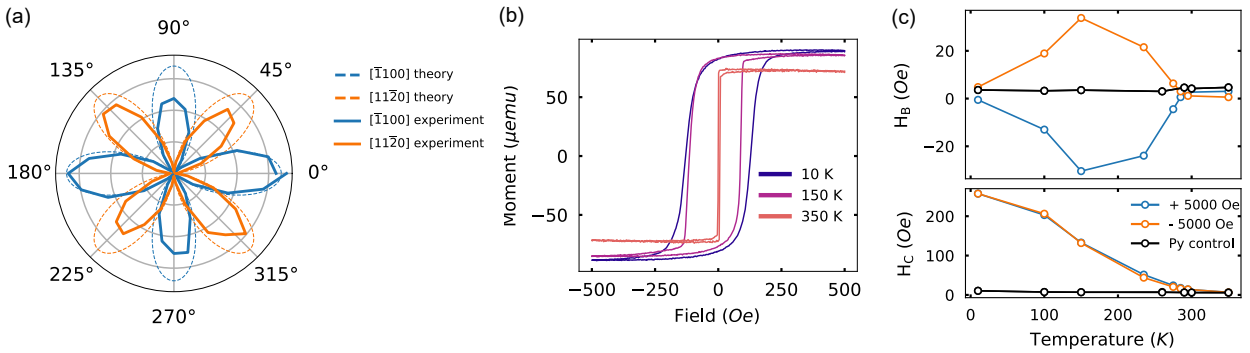

Figure 4.4.1: (a) Optical second harmonic generation intensity from a 30-nm-thick Cr_2O_3 on V_2O_3 electrode at room temperature (orange: analyzer along the x-direction ([11$\bar{2}$0]), blue: analyzer along y-direction ([$\bar{1}$100])) and theoretical plot of electric dipole signal (Equation (4.4.0.2)) when analyzer is fixed along x-direction (dash-orange) and y-direction (dash-blue) showing the agreement between experimental result and theory. **(b)** Broadening of coercive field of Permalloy in the heterostructure Pt (5 nm)/Permalloy (Py) (4nm)/Cr_2O_3 (30 nm)/V_2O_3/Al_2O_3 at low temperatures. **(c)** Exchange bias field (top panel) and coercive field (bottom panel) as a function of temperature for Pt (5 nm)/Permalloy (Py) (4 nm)/Cr_2O_3 (30 nm)/V_2O_3/Al_2O_3 and control sample Pt (5 nm)/Py (4 nm)/Al_2O_3 heterostructures. The control data of permalloy shows both $\pm$5000 Oe cooling field scans. Adapted from [21].

Pt layer is then etched into Hall bar cross with different sizes. Figure 4.5.1(a) shows the asymmetric error coming from the misalignment of electrodes. Figure 4.5.1(b) illustrates the effect of temperature drift in Pt that contributes to signal error in anomalous Hall voltage. After adapting signal correction method mentioned in **Chapter 2**, a small offset still exists (Figure 4.5.1(c)). This error is a contribution from the uncertainty of the sourcemeter that can not be canceled within the measurement setup.

The anomalous Hall signal at zero applied magnetic field as a function of temperature is explored next. This experiment is performed in the PPMS Dynacool system. The Cr_2O_3 sample is annealed in $\pm$1 Tesla from 400 down to 200 K to form mono magnetic domain. Figure 4.5.2(a) shows raw data that reflects the error offset due to the uncertainty of the equipment. Figure 4.5.2(b) shows the shifted data which reveals the temperature when the

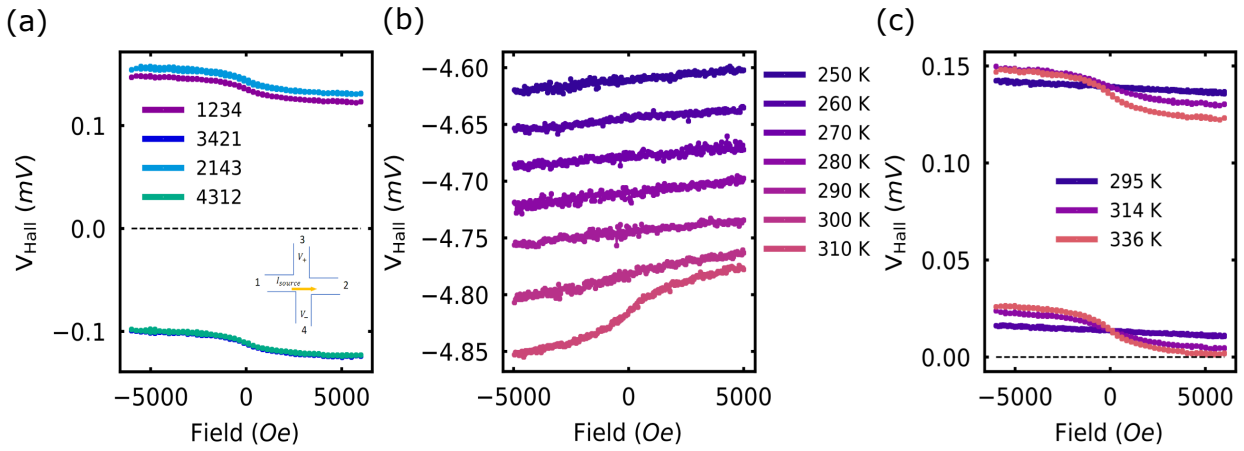

Figure 4.5.1: **(a)** Raw anomalous Hall signals without any correction for each configuration shows error coming from asymmetric contacts. **(b)** Raw anomalous Hall signals at different temperatures shows temperature drifts. **(c)** After signal correction using spinning current offset, the offset due to instrument uncertainty.

anomalous Hall signal disappear (or becomes constant) is $323\,K$. This is indeed the Néel temperature of the heterostructure, which is higher than that of a $250\,nm$ thick Cr_2O_3 reported in literature ($\sim 301\,K$, Figure 4.1.3(c)).[23]

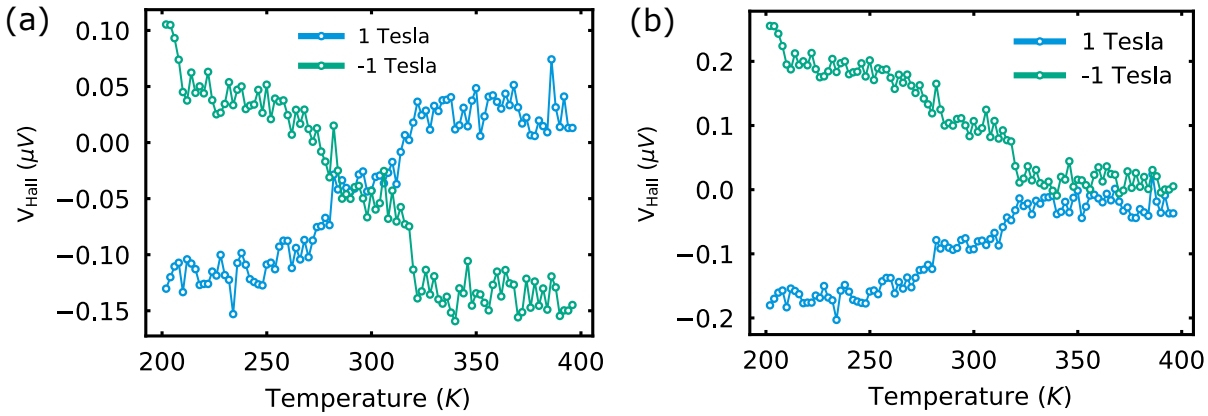

Figure 4.5.2: **(a)** Anomalous Hall signal as a function of temperature, raw data. **(b)** Anomalous Hall signal as a function of temperature, shifted data to remove error from instrument uncertainty.

In summary, by taking advantage of isostructural growth with minimal strain coming from the electrode, single crystal thin film Cr_2O_3 is fabricated successfully with magneto-electric order at room temperature for thickness as low as $30\,nm$. At $60\,nm$, not only the film exhibits bulk like resistivity behaviour, but also demonstrates an enhancement in the operating temperature up to $323\,K$ compared to the bulk value ($308\,K$). In the next chapter, I will discuss the challenge in improving the Néel temperature further as well as perspective on electric field switching of magnetization.

Chapter 5

Conclusions and Recommendations for Future Work

Using an isostructural oxide electrode V_2O_3 with minimal lattice mismatch, high quality single crystal thin films of Cr_2O_3 have been achieved at sub-100 nm thicknesses. Leakage measurements and electric breakdown tests are performed in thin film at thickness as low as 30 nm, showing a significant improvement in dielectric properties compared to thin films with crystallographic twinned domains. Magnetoelectric symmetry at room temperature is found to exist in film at thickness of 30 nm with improved blocking temperature in an exchange bias system. At 60 nm, the film exhibits bulk like resistivity and a breakdown field in the range of 150 to 300 MV/m. Furthermore, the Néel temperature at this thickness is found to be 15 K higher than the bulk value (308 K), an improvement that results from epitaxial strain alone without the support from elemental doping. Magnetization reversal through magnetic field annealing shows promises for future electric field control of magnetization, but also raises a challenge in bringing the film to mono-domain state to maximize switching efficiency and improve signal detection.

For practical applications in high temperature computing, higher Néel temperature is needed. Previous studies have shown the potential of Boron doping in improving the working temperature up to 400 K.[75] However, the controversy over the effect of Boron doping on

dielectric properties of Cr_2O_3 has not been resolved, which will be discussed in this chapter. Additionally, from the scaling point of view, signal detection in Cr_2O_3 switching is a major topic in designing measurement setup that would increase the complexity of the circuit board. This chapter will also discuss the signal level that should be expected in this system as well as potential ways to improve this signal detection.

5.1 Boron doping of Cr_2O_3

The doping of Boron in thin film Cr_2O_3 is performed using Boron-doped Cr_2O_3 target purchased from Lesker. The Boron concentration in the target is 30 % (atomic). Due to the low melting temperature of B_2O_3 ($450\,^oC$), the density of the Boron doped target is much smaller than the pure target (only 53.6% of theoretical value). The growth condition is adjusted accordingly to accomodate the change in composition and density of the target to achieve comparable quality as the pure thin film. Figure 5.1.1(a) shows the X-ray diffraction data of Boron-doped Cr_2O_3 with and without V_2O_3 electrode. There is a shift in Boron-doped Cr_2O_3 peak compared to the pure sample, indicating larger strain contributed from Boron presence in the lattice. The existence of Boron in deposited film is further confirmed by XPS, showing a very clear signal of B^{3+} (Figure 5.1.1(b)) with estimated concentration of Boron between 10 to 15%.

The Boron doped thin film shows a detectable resistance just by a handheld multimeter ($\sim 4\,M\Omega$). Detailed dielectric behaviour of the sample is characterized using the Keithley sourcemeter, which is shown in Figure 5.1.1(c). The IV curve exhibits semiconductor-like behavior without breakdown characteristics often seen in insulators. The leakage current reaches a very high value (tens of milliampere) without device breaking down. This behaviour is similar to previous report in literature (Figure 5.1.2(b)) (in which a $200\,nm$ thick Boron doped thin film was under investigation).[25] A possible explanation can be proposed using the calculated Density of States in Boron doped Cr_2O_3 (Figure 5.1.2(a)). The introduction of an impurity level near the Fermi level increases the chance for Cr_2O_3 to be come conducting.

This argument, however, is not solid. Detailed calculation of defect formation energy for Boron-doped Cr_2O_3 is underway to confirm this hypothesis.

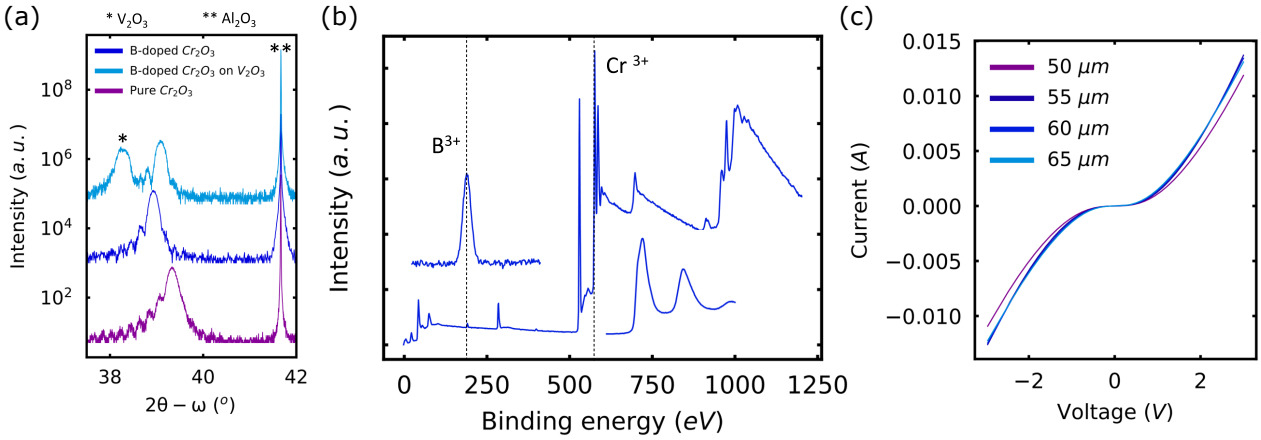

Figure 5.1.1: **(a)** X-ray diffraction of Boron-doped Cr_2O_3 grown on (0001) Al_2O_3 and V_2O_3 electrode, in comparison with pure Cr_2O_3 grown on bare (0001) Al_2O_3. **(b)** Boron detection of Boron doped Cr_2O_3 grown on Al_2O_3 using XPS. **(c)** Dielectric behaviour of Boron-doped Cr_2O_3 grown on V_2O_3 electrode, the estimated thickness is in the range of ~ 55 to $60\,nm$.

Based on these initial findings, it is recommended that future works can explore:

- Defect formation energy for Boron-doped Cr_2O_3 is needed to confirm the observed semiconducting behaviors.
- Néel temperature of the Boron-doped series needs to be confirmed by second harmonic generation and electrical detection.
- Detection of blocking temperature should be done (using a similar heterostructure with permalloy for benchmarking with the current work).

5.2 Electrical switching in sub 100-nm-thin Cr_2O_3

Electrical switching potential in the investigated system needs to be evaluated. The change in anomalous Hall signal with applied electric field has not been detected. This can be

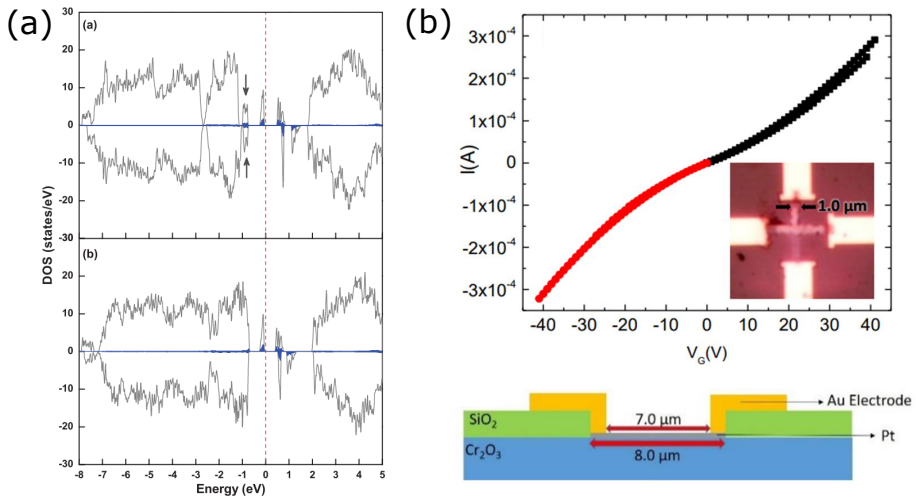

Figure 5.1.2: **(a)** Density functional theory calculation of density of state (DOS) for B impurity in Cr_2O_3, with the normal number of electron (top panel) and in the Slater transition state (bottom panel). The dashed line is Fermi level, while the black line is the total DOS and the blue shaded area is the local DOS for Boron impurity. Printed with permission from [24]. **(b)** Electrical behaviour of 200 nm Boron-doped thin film, adapted from [25].

accounted for by domain pinning at low thickness, the switching voltage being higher than the breakdown value or the limitation of the measurement setup. A closer look at the error in detected anomalous Hall signal versus temperature reveals a noise level of $\sim$ 50 nV. From previous report of Kosub *et al.* (2017), the difference in voltage signal of up and down state is $\Delta V = 180\,nV$ (Figure 5.2.1), which is about 12% of the possible switched domains (calculated from temperature dependence of anomalous Hall signal in Figure 4.1.3(c)). Using this ratio, the change in amplitude if switching happens in the 60 nm thick film will be in the range of 12 nV, which is lower than the noise level. Therefore, the switching could not be detectable using the current setup. This can only be overcome by: **1** Increase the net magnetization through the annealing process and **2** Improve the measurement setup using Delta mode in the nanovoltmeter in combination with the sourcemeter to reach 5 nV error level. This Delta mode should not be used with the matrix card since it would also increase the noise level. Furthermore, this poses a new challenge in practical application of Cr_2O_3, which is the complication of the signal detection setup for such an ultra-low signal change.

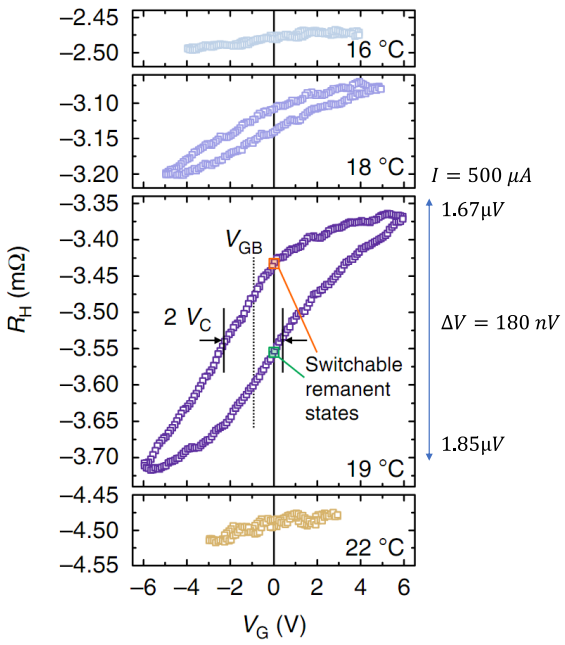

Figure 5.2.1: Isothermal switching of 200 nm thick Cr_2O_3 film showing switching characteristics at certain temperature. Adapted from [14].

Recommended future works based on the above results are:

1. Improvement of the measurement setup using delta mode is needed.

2. Electric field switching tests can be performed on magnetic field/magneto-electric field annealed samples and on pristine samples.

3. The search for stronger spin-orbit coupling materials as alternative for Pt will be beneficial for stronger detection signal.

Bibliography

[1] Jordan M. Horowitz. Computing's energy problem (and what can we do about it). *Digest of Technical Papers - IEEE International Solid-State Circuits Conference*, 57, 2014.

[2] J. Stohr and H. C. Siegmann, editors. *Magnetism: From Fundamentals to Nanoscale Dynamics*. Springer, 2006.

[3] J. M. D. Coey. *Magnetism and Magnetic Materials*. Cambridge University Press, 2010.

[4] T. Ashida, M. Oida, N. Shimomura, T. Nozaki, T. Shibata, and M. Sahashi. Isothermal electric switching of magnetization in Cr_2O_3/Co thin film system. *Applied Physics Letters*, 106(13):132407, 2015.

[5] Congli Sun, Zhewen Song, Ashutosh Rath, Michael Street, William Echtenkamp, Jie Feng, Christian Binek, Dane Morgan, and Paul Voyles. Local Dielectric Breakdown Path along c-Axis Planar Boundaries in Cr_2O_3 Thin Films. *Advanced Materials Interfaces*, 4(20):1700172, 2017.

[6] M. Trassin, N. Viart, C. Ulhaq-Bouillet, G. Versini, S. Barre, C. Leuvrey, and G. Pourroy. Ultraflat monocrystalline Pt (111) electrodes. *Journal of Applied Physics*, 105(10), 2009.

[7] P. B. Meisenheimer, T. J. Kratofil, and J. T. Heron. Giant enhancement of exchange coupling in entropy-stabilized oxide heterostructures. *Scientific Reports*, 7(1):1–6, 2017.

[8] K. N. Tu, James W. Mayer, and Leonard C. Feldman. *Electronic thin film science : for electrical engineers and materials scientists*. 1992.

[9] George H. Gilmer and Marcia H. Grabow. Models of Thin Film Growth Modes. *JOM 1987 39:6*, 39(6):19–23, 2012.

[10] Hangwen Guo, Dali Sun, Wenbin Wang, Zheng Gai, Ivan Kravchenko, Jian Shao, Lu Jiang, Thomas Z. Ward, Paul C. Snijders, Lifeng Yin, Jian Shen, and Xiaoshan Xu. Growth diagram of $La_{0.7}Sr_{0.3}MnO_3$ thin films using pulsed laser deposition. *Journal of Applied Physics*, 113(23):234301, 2013.

[11] Jianwei Meng, Zhihui Chen, and Anquan Jiang. Investigation of the growth mechanism of $SrRuO_3$ thin films fabricated by pulsed laser deposition. *Japanese Journal of Applied Physics*, 54(5):055502, 2015.

[12] Rigaku. *X-ray diffraction analysis for thin film samples*. Rigaku Corporation.

[13] Miho Yasaka. X-ray thin-film measurement techniques: X-ray reflectivity measurement. *The Rigaku Journal,*, 26(2), 2010.

[14] Tobias Kosub, Martin Kopte, Ruben Hühne, Patrick Appel, Brendan Shields, Patrick Maletinsky, René Hübner, Maciej Oskar Liedke, Jürgen Fassbender, Oliver G. Schmidt, and Denys Makarov. Purely antiferromagnetic magnetoelectric random access memory. *Nature Communications*, 8:13985, 2017.

[15] G. Bauer, J. H. Li, and V. Holy. High Resolution X-Ray Reciprocal Space Mapping. *Acta Physica Polonica A. Proceedings of the II hit. School and Symposium on Physics in Materials Science*, 89:115–127, 1996.

[16] W. X. Ni, K. Lyutovich, J. Alami, C. Tengstedt, M. Bauer, and E. Kasper. X-ray reciprocal space mapping studies of strain relaxation in thin SiGe layers ($\geq 100\,nm$) using a low temperature growth step. *Journal of Crystal Growth*, 227-228:756–760, 2001.

[17] A. O. Adeyeye and G. Shimon. Growth and Characterization of Magnetic Thin Film and Nanostructures. In Robert E. Camley, Zbigniew Celinski, and Robert L. Stamps, editors, *Handbook of Surface Science*, volume 5, chapter 1, pages 1–41. North-Holland, 2015.

[18] Jeffrey Lindemuth. *Hall Effect Measurement Handbook: A Fundamental Tool for Semiconductor Material Characterization.* Lake Shore Cryontronics, Incorporated, 2020, 2020.

[19] Johanna Nordlander, Gabriele De Luca, Nives Strkalj, Manfred Fiebig, and Morgan Trassin. Probing Ferroic States in Oxide Thin Films Using Optical Second Harmonic Generation. *Applied Sciences*, 8(4):570, 2018.

[20] Nguyen M. Vu, Peter B. Meisenheimer, and John T. Heron. Tunable magnetoelastic anisotropy in epitaxial (111) $Tm_3Fe_5O_{12}$ thin films. *Journal of Applied Physics*, 127(15):153905, 2020.

[21] N. M. Vu, X. Luo, S. Novakov, W. Jin, J. Nordlander, P. B. Meisenheimer, M. Trassin, L. Zhao, and J. T. Heron. Bulk-like dielectric and magnetic properties of sub 100 nm thick single crystal Cr_2O_3 films on an epitaxial oxide electrode. *Scientific Reports 2020 10:1*, 10(1):1–6, 2020.

[22] Xi He, Yi Wang, Ning Wu, Anthony N. Caruso, Elio Vescovo, Kirill D. Belashchenko, Peter A. Dowben, and Christian Binek. Robust isothermal electric control of exchange bias at room temperature. *Nature Materials*, 9(7):579–585, 2010.

[23] Tobias Kosub, Martin Kopte, Florin Radu, Oliver G. Schmidt, and Denys Makarov. All-Electric Access to the Magnetic-Field-Invariant Magnetization of Antiferromagnets. *Physical Review Letters*, 115(9):097201, 2015.

[24] Sai Mu, A. L. Wysocki, and K. D. Belashchenko. Effect of substitutional doping on the Néel temperature of Cr_2O_3. *Physical Review B - Condensed Matter and Materials Physics*, 87(5):1–11, 2013.

[25] Ather Mahmood, Will Echtenkamp, Mike Street, Jun-Lei Wang, Shi Cao, Takashi Komesu, Peter A. Dowben, Pratyush Buragohain, Haidong Lu, Alexei Gruverman, Arun Parthasarathy, Shaloo Rakheja, and Christian Binek. Voltage controlled Néel vector rotation in zero magnetic field. *Nature Communications 2021 12:1*, 12(1):1–8, 2021.

[26] Douglas B. Chrisey and Graham K. Hubler, editors. *Pulsed Laser Deposition of Thin Films*. John Wiley & Sons, Inc., 1994.

[27] A. Paoletti, editor. *Physics of magnetic garnets*. Italian Physical Society, 1978.

[28] Sasikanth Manipatruni, Dmitri E. Nikonov, Chia Ching Lin, Tanay A. Gosavi, Huichu Liu, Bhagwati Prasad, Yen Lin Huang, Everton Bonturim, Ramamoorthy Ramesh, and Ian A. Young. Scalable energy-efficient magnetoelectric spin–orbit logic. *Nature*, 565(7737):35–42, 2019.

[29] Gordon E. Moore. Cramming more components onto integrated circuits. *Proceedings of the IEEE*, 86(1):82–85, 1998.

[30] Nicola Jones. How to stop data centres from gobbling up the world's electricity. *Nature*, 561(7722):163–166, 2018.

[31] N. A. Spaldin and R. Ramesh. Advances in magnetoelectric multiferroics. *Nature Materials 2019 18:3*, 18(3):203, 2019.

[32] Peter B. Meisenheimer, Steve Novakov, Nguyen M. Vu, and John T. Heron. Perspective: Magnetoelectric switching in thin film multiferroic heterostructures. *Journal of Applied Physics*, 123(24):240901, 2018.

[33] D. C. Ralph and M. D. Stiles. Spin transfer torques. *Journal of Magnetism and Magnetic Materials*, 320:1190–1216, 2008.

[34] Harry Suhl. *IEEE Transactions on Magnetics*.

[35] Aidan J. Lee, Jack T. Brangham, Yang Cheng, Shane P. White, William T. Ruane, Bryan D. Esser, David W. McComb, P. Chris Hammel, and Fengyuan Yang. Metallic ferromagnetic films with magnetic damping under 1.4 10 3. *Nature Communications*, 8(1):1–6, 2017.

[36] Movaffaq Kateb and Snorri Ingvarsson. Thickness-dependent magnetic and magnetoresistance properties of permalloy prepared by field assisted tilt sputtering. *SAS 2017 - 2017 IEEE Sensors Applications Symposium, Proceedings*, 2017.

[37] Movaffaq Kateb and Snorri Ingvarsson. Correlation of uniaxial magnetic anisotropy axes and principal resistivities in polycrystalline ferromagnetic films. *Journal of Magnetism and Magnetic Materials*, 532:167982, 2021.

[38] Kevin Garello, Can Onur Avci, Ioan Mihai Miron, Manuel Baumgartner, Abhijit Ghosh, Stéphane Auffret, Olivier Boulle, Gilles Gaudin, and Pietro Gambardella. Ultrafast magnetization switching by spin-orbit torques. *Applied Physics Letters*, 105(21):212402, 2014.

[39] Chi Tang, Yawen Liu, Zilong Jiang, Jing Shi, Cui-Zu Chang, Jagadeesh S. Moodera, Chao-Xing Liu, Gejian Zhao, Martha R. McCartney, David J. Smith, and Tingyong Chen. Above 400-K robust perpendicular ferromagnetic phase in a topological insulator. *Science Advances*, 3(6):2–6, 2017.

[40] Andy Quindeau, Can O. Avci, Wenqing Liu, Congli Sun, Maxwell Mann, Astera S. Tang, Mehmet C. Onbasli, David Bono, Paul M. Voyles, Yongbing Xu, Jason Robinson, Geoffrey S.D. Beach, and Caroline A. Ross. $Tm_3Fe_5O_{12}$/Pt Heterostructures with Perpendicular Magnetic Anisotropy for Spintronic Applications. *Advanced Electronic Materials*, 3(1), 2017.

[41] C. N. Wu, C. C. Tseng, K. Y. Lin, C. K. Cheng, S. L. Yeh, Y. T. Fanchiang, M. Hong, and J. Kwo. High-quality single-crystal thulium iron garnet films with perpendicular magnetic anisotropy by off-axis sputtering. *AIP Advances*, 8(5), 2018.

[42] Can Onur Avci, Andy Quindeau, Chi Feng Pai, Maxwell Mann, Lucas Caretta, Astera S. Tang, Mehmet C. Onbasli, Caroline A. Ross, and Geoffrey S.D. Beach. Current-induced switching in a magnetic insulator. *Nature Materials*, 16(3):309–314, 2017.

[43] Jeongchun Ryu, Soogil Lee, Kyung-Jin Lee, and Byong-Guk Park. Current-Induced Spin–Orbit Torques for Spintronic Applications. *Advanced Materials*, 32(35):1907148, 2020.

[44] Daniele Gastaldo, Nikita Strelkov, Liliana D. Buda-Prejbeanu, Bernard Dieny, Olivier Boulle, Paolo Allia, and Paola Tiberto. Impact of Dzyaloshinskii-Moriya interactions on the thermal stability factor of heavy metal/magnetic metal/oxide based nano-pillars. *Journal of Applied Physics*, 126(10):103905, 2019.

[45] J. T. Heron, J. L. Bosse, Q. He, Y. Gao, M. Trassin, L. Ye, J. D. Clarkson, C. Wang, Jian Liu, S. Salahuddin, D. C. Ralph, D. G. Schlom, J. Íñiguez, B. D. Huey, and R. Ramesh. Deterministic switching of ferromagnetism at room temperature using an electric field. *Nature 2014 516:7531*, 516(7531):370, 2014.

[46] Jon F. Ihlefeld, David T. Harris, Ryan Keech, Jacob L. Jones, Jon Paul Maria, and Susan Trolier-McKinstry. Scaling Effects in Perovskite Ferroelectrics: Fundamental Limits and Process-Structure-Property Relations. *Journal of the American Ceramic Society*, 99(8):2537–2557, 2016.

[47] Y. Ji, J. Miao, Y. M. Zhu, K. K. Meng, X. G. Xu, J. K. Chen, Y. Wu, and Y. Jiang. Negative spin Hall magnetoresistance in antiferromagnetic Cr_2O_3/Ta bilayer at low temperature region. *Appl. Phys. Lett*, 112:232404, 2018.

[48] Yang Cheng, Sisheng Yu, Menglin Zhu, Jinwoo Hwang, and Fengyuan Yang. Evidence of the Topological Hall Effect in Pt/Antiferromagnetic Insulator Bilayers. *Physical Review Letters*, 123:237206, 2019.

[49] Satischandra B. Ogale, editor. *Thin Films and Heterostructures for Oxide Electronics*. Springer-Verlag, 2005.

[50] Robert Eason, editor. *Pulsed Laser Deposition of Thin Films: Applications-Led Growth of Functional Materials*. Wiley-Interscience, 2006.

[51] Shalini Kumari, Navid Mottaghi, Chih-Yeh Huang, Robbyn Trappen, Ghadendra Bhandari, Saeed Yousefi, Guerau Cabrera, Mohindar S. Seehra, and Mikel B. Holcomb. Effects of Oxygen Modification on the Structural and Magnetic Properties of Highly Epitaxial $La_{0.7}Sr_{0.3}MnO_3$ (LSMO) thin films. *Scientific Reports 2020 10:1*, 10(1):1–11, 2020.

[52] M. Kubota, K. Shibuya, Y. Tokunaga, F. Kagawa, A. Tsukazaki, Y. Tokura, and M. Kawasaki. Systematic control of stress-induced anisotropy in pseudomorphic iron garnet thin films. *Journal of Magnetism and Magnetic Materials*, 339:63–70, 2013.

[53] Dong Hun Kim, Nicolas M. Aimon, Lei Bi, J. M. Florez, Gerald F. Dionne, and C. A. Ross. Magnetostriction in epitaxial $SrTi_{1-x}Fe_xO_{3-\delta}$ perovskite films with x = 0.13 and 0.35. *Journal of Physics Condensed Matter*, 25(2), 2013.

[54] Jia-Mian Hu and C. W. Nan. Electric-field-induced magnetic easy-axis reorientation in ferromagnetic/ferroelectric layered heterostructures. *Physical Review B*, 80(22):224416, 2009.

[55] I. Dzyaloshinskii. On the magneto-electrical effect in antiferromagnets. *Journal of Experimental and Theoretical Physics (U.S.S.R)*, 37:881–882, 1959.

[56] D. N. Astrov. Magnetoelectric effect in chromium oxide. *Soviet Physics JETP*, 13(4), 1961.

[57] Hans Schmid. Magnetoelectric effects in insulating magnetic materials. *Complex Mediums*, 4097(30):12–24, 2000.

[58] Ch Binek and B Doudin. Magnetoelectronics with magnetoelectrics. *Journal of Physics: Condensed Matter*, 17(2):L39, 2004.

[59] Manuel Bibes and Agnès Barthélémy. Towards a magnetoelectric memory. *Nature Materials 2008 7:6*, 7(6):425–426, 2008.

[60] J.-P. Rivera. On definitions, units, measurements, tensor forms of the linear magnetoelectric effect and on a new dynamic method applied to Cr-Cl boracite. *Ferroelectrics*, 161(1):165–180, 1994.

[61] Luca Corbellini, Christian Lacroix, Catalin Harnagea, Andreas Korinek, Gianluigi A. Botton, David Ménard, and Alain Pignolet. Epitaxially stabilized thin films of ϵ-Fe_2O_3 (001) grown on YSZ (100). *Scientific Reports 2017 7:1*, 7(1):1–9, 2017.

[62] Florin Radu and Hartmut Zabel. Exchange Bias Effect of Ferro-/Antiferromagnetic Heterostructures. In *Magnetic Heterostructures*, pages 97–184. Springer Berlin Heidelberg, Berlin, Heidelberg, 2008.

[63] P. K. Manna and S. M. Yusuf. Two interface effects: Exchange bias and magnetic proximity. *Physics Reports*, 535(2):61–99, 2014.

[64] M. Ali, C. H. Marrows, M. Al-Jawad, B. J. Hickey, A. Misra, U. Nowak, and K. D. Usadel. Antiferromagnetic layer thickness dependence of the IrMn/Co exchange-bias system. *Physical Review B*, 68(21):214420, 2003.

[65] G. Scholten, K. D. Usadel, and U. Nowak. Coercivity and exchange bias of ferromagnetic/antiferromagnetic multilayers. *Physical Review B*, 71(6):064413, 2005.

[66] Wei Yuan, Qiong Zhu, Tang Su, Yunyan Yao, Wenyu Xing, Yangyang Chen, Yang Ma, Xi Lin, Jing Shi, Ryuichi Shindou, X. C. Xie, and Wei Han. Experimental signatures of spin superfluid ground state in canted antiferromagnet Cr_2O_3 via nonlocal spin transport. *Science Advances*, 4(4):eaat1098, 2018.

[67] Justin S. Brockman, Li Gao, Brian Hughes, Charles T. Rettner, Mahesh G. Samant, Kevin P. Roche, and Stuart S.P. Parkin. Subnanosecond incubation times for electric-

field-induced metallization of a correlated electron oxide. *Nature Nanotechnology*, 9(6):453–458, 2014.

[68] Joe Sakai, Patrice Limelette, and Hiroshi Funakubo. Transport Properties and c/a Ratio of V_2O_3 Thin Films Grown on c- and r-Plane Sapphire Substrates by Pulsed Laser Deposition. *Applied Physics Letters*, 107(24):241901, 2015.

[69] Einar B. Thorsteinsson, Seyedmohammad Shayestehaminzadeh, and Unnar B. Arnalds. Tuning metal-insulator transitions in epitaxial V_2O_3 thin films. *Applied Physics Letters*, 112(16):161902, 2018.

[70] Congli Sun, Michael Street, Ryan Jacobs, Dane Morgan, Paul M. Voyles, and Christian Binek. Identification and Quantification of Boron Dopant Sites in Antiferromagnetic Cr_2O_3 Films by Electron Energy Loss Spectroscopy . *Microscopy and Microanalysis*, 23(S1):1584–1585, 2017.

[71] M. Fiebig, D. Fröhlich, B. B. Krichevtsov, and R. V. Pisarev. Second harmonic generation and magnetic-dipole-electric-dipole interference in antiferromagnetic Cr_2O_3. *Physical Review Letters*, 73(15):2127–2130, 1994.

[72] Manfred Fiebig, Victor V. Pavlov, and Roman V. Pisarev. Second-harmonic generation as a tool for studying electronic and magnetic structures of crystals: review. *Journal of the Optical Society of America B*, 22(1):96, 2005.

[73] Hans-Joachim Freund, Helmut Kuhlenbeck, and Volker Staemmler. Oxide surfaces. *Reports on Progress in Physics*, 59(3):283, 1996.

[74] Wolfgang Kleemann and Christian Binek. Multiferroic and Magnetoelectric Materials. pages 163–187. 2013.

[75] M. Street, W. Echtenkamp, T. Komesu, S. Cao, P. A. Dowben, and C. Binek. Increasing the Néel temperature of magnetoelectric chromia for voltage-controlled spintronics. *Applied Physics Letters*, 104(22), 2014.